Contribution of the world's main dust source regions to the global cycle of desert dust

Jasper F. Kok[1], Adeyemi A. Adebiyi[1], Samuel Albani[2,3], Yves Balkanski[3], Ramiro Checa-Garcia[3], Mian Chin[4], Peter R. Colarco[4], Douglas S. Hamilton[5], Yue Huang[1], Akinori Ito[6], Martina Klose[7], Longlei Li[5], Natalie M. Mahowald[5], Ron L. Miller[8], Vincenzo Obiso[7,8], Carlos Pérez García-Pando[7,9], Adriana Rocha-Lima[10,11], and Jessica S. Wan[5]

[1]Department of Atmospheric and Oceanic Sciences, University of California, Los Angeles, CA 90095, USA
[2]Department of Environmental and Earth Sciences, University of Milano-Bicocca, Milano, Italy
[3]Laboratoire des Sciences du Climat et de l'Environnement, CEA-CNRS-UVSQ-UPSaclay, Gif-sur-Yvette, France
[4]Atmospheric Chemistry and Dynamics Laboratory, NASA Goddard Space Flight Center, Greenbelt, MD 20771, USA
[5]Department of Earth and Atmospheric Sciences, Cornell University, Ithaca, NY 14850, USA
[6]Yokohama Institute for Earth Sciences, JAMSTEC, Yokohama, Kanagawa 236-0001, Japan
[7]Barcelona Supercomputing Center (BSC), 08034 Barcelona, Spain
[8]NASA Goddard Institute for Space Studies, New York NY10025 USA
[9]ICREA, Catalan Institution for Research and Advanced Studies, 08010 Barcelona, Spain
[10]Physics Department, UMBC, Baltimore, Maryland, USA
[11]Joint Center Joint Center for Earth Systems Technology, UMBC, Baltimore, Maryland, USA

Correspondence to: Jasper F. Kok (jfkok@ucla.edu)

Abstract. Even though desert dust is the most abundant aerosol by mass in Earth's atmosphere, the relative contributions of the world's major dust source regions to the global dust cycle remain poorly constrained. This problem hinders accounting for the potentially large impact of regional differences in dust properties on clouds, the Earth's energy balance, and terrestrial and marine biogeochemical cycles. Here, we constrain the contribution of each of the world's main dust source regions to the global dust cycle. We use an analytical framework that integrates an ensemble of global model simulations with observationally informed constraints on the dust size distribution, extinction efficiency, and regional dust aerosol optical depth. We obtain a data set that constrains the relative contribution of each of nine major source regions to size-resolved dust emission, atmospheric loading, optical depth, concentration, and deposition flux. We find that the 22-29 Tg (one standard error range) global loading of dust with geometric diameter up to 20 μm is partitioned as follows: North African source regions contribute ~50% (11-15 Tg), Asian source regions contribute ~40% (8-13 Tg), and North American and Southern Hemisphere regions contribute ~10% (1.8-3.2 Tg). Current models might on average be overestimating the contribution of North African sources to atmospheric dust loading at ~65%, while underestimating the contribution of Asian dust at ~30%. However, both our results and current models could be affected by unquantified biases, such as due to errors in separating dust aerosol optical depth from that produced by other aerosol species in remote sensing retrievals in poorly observed desert regions. Our results further show that each source region's dust loading peaks in local spring and summer, which is partially driven by increased dust lifetime

in those seasons. We also quantify the dust deposition flux to the Amazon rainforest to be ~10 Tg/year, which is a factor of 2-

35 3 less than inferred from satellite data by previous work that likely overestimated dust deposition by underestimating the dust mass extinction efficiency. The data obtained in this paper can be used to obtain improved constraints on dust impacts on clouds, climate, biogeochemical cycles, and other parts of the Earth system.

1 Introduction

40 Desert dust is likely the most abundant aerosol type by mass (Kinne et al., 2006; Kok et al., 2017) and produces a range of important impacts on the Earth system, including on clouds, the Earth's energy and water budgets, and biogeochemical cycles (Shao et al., 2011; Mahowald et al., 2014; Miller et al., 2014). These impacts are spatially heterogeneous, not only because dust loading itself varies substantially between regions, but also because the properties of dust depend on mineralogy, which varies with the region of origin (Claquin et al., 1999; Grousset and Biscaye, 2005; Journet et al., 2014). Consequently,

45 determining dust impacts on the Earth system requires not only constraints on global dust loading (Huneeus et al., 2011; Kok et al., 2017), but also on the emission, loading, and deposition generated by individual source regions. However, estimates of the contributions of the world's major source regions to the global dust cycle diverge widely. For instance, model estimates of emissions from the main source regions vary by up to an order of magnitude between different global model simulations (Huneeus et al., 2011; Wu et al., 2020).

50

There are several reasons why this poor understanding of the contribution of each source region to the global dust cycle hinders quantification of dust impacts on the Earth system. First, since dust loading is spatially heterogeneous, constraining regional dust loading is a prerequisite to constraining dust impacts on regional climate, weather, air quality, and the hydrological cycle (Seinfeld et al., 2004; Engelstaedter et al., 2006; Huang et al., 2014; Vinoj et al., 2014; Sharma and Miller, 2017; Kok et al.,

55 2018). Second, dust deposition records indicate that atmospheric dust loading has been highly variable, both between glacial and interglacial periods and from pre-industrial to modern times (Petit et al., 1999; McConnell et al., 2007; Albani et al., 2018; Hooper and Marx, 2018). Inferring the impacts of these large changes in dust loading on the Earth system requires knowledge of the origin of dust deposited to each measurement site (Mahowald et al., 2010). Finally, many dust impacts on the Earth system are sensitive to dust mineralogy, which varies both within and between major source regions (Biscaye, 1965; Claquin

60 et al., 1999; Di Biagio et al., 2017). Examples of dust impacts that are sensitive to mineralogy include dust direct radiative effects (Balkanski et al., 2007; Perlwitz et al., 2015b; Scanza et al., 2015; Di Biagio et al., 2019), dust interactions with clouds through dust serving as ice nuclei (Atkinson et al., 2013; Shi and Liu, 2019), and dust impacts on biogeochemistry through the deposition of micronutrients such as iron and phosphorus (Swap et al., 1992; Jickells et al., 2005; Journet et al., 2008; Schroth et al., 2009). Since dust has potentially doubled since pre-industrial times (Mahowald et al., 2010; Hooper and Marx, 2018),

65 some of these effects might have produced a marine biogeochemical response (Hamilton et al., 2020; Ito et al., 2020) that

might have resulted in a substantial global indirect radiative forcing (Mahowald, 2011). As such, constraining source-specific dust emissions and loading is critical to constraining global climate sensitivity (Andreae et al., 2005; Kiehl, 2007).

Many past studies of the contributions of the main dust source regions to the global dust cycle have been based on global model simulations (Tanaka and Chiba, 2006; Chin et al., 2007; Huneeus et al., 2011; Wu et al., 2020). These simulations exhibit substantial biases when compared to observations of dust abundance and of dust microphysical properties like size distribution and mass extinction efficiency (Kok et al., 2014a; Ansmann et al., 2017; Adebiyi et al., 2020; Checa-Garcia et al., 2020). Recognizing this problem, Ginoux et al. (2012) made an important advance towards more accurate constraints on the regional contributions to the global dust cycle by using extensive dust aerosol optical depth data from the Moderate Resolution Imaging Spectroradiometer (MODIS) Deep Blue algorithm to obtain a fine-grained map of the frequency of activation of dust sources. They then used this result to scale emissions in a global model simulation tuned to a specific global emission rate (1223 Tg/year for dust up to 12 μm diameter) obtained in a previous modeling study (Ginoux et al., 2001), thereby obtaining results for the emission rate generated by each main source region. Another recent study by Albani et al. (2014) regionally tuned model sources to match concentration, deposition, and aerosol optical depth observations using optimal estimation combined with expert opinion to incorporate geochemical tracer information in dust deposition measurements (Albani et al., 2014). Although both these studies are steps towards obtaining more reliable constraints on the contribution of each main source region to the global dust cycle, remaining deficiencies include (1) substantial biases in dust microphysical properties such as size distribution and extinction efficiency (Adebiyi and Kok, 2020; Adebiyi et al., 2020), (2) the use of a single model to represent dust transport and emission even though the spread in predictions between models is large (Huneeus et al., 2011; Checa-Garcia et al., 2020; Wu et al., 2020), and (3) the lack of robust uncertainty estimates in the contributions of the different source regions that can be propagated into calculated dust impacts such as dust radiative forcing. As such, although clear progress has been made in understanding the relative contributions of the world's source regions to the global dust cycle, current knowledge is not yet sufficient to constrain regionally varying dust impacts or to reliably inform the provenance of dust in deposition records.

Here we obtain improved constraints on the contributions from the world's main dust source regions to the global cycle of desert dust. We do so in Section 2 by building on the improved representation of the global dust cycle that we obtained in a companion paper (Kok et al., in review) by integrating an ensemble of global model simulations with observational constraints on the properties and abundance of atmospheric dust. We obtain a data set that constrains the contributions of each of nine major source regions to size-resolved dust emission, loading, dust aerosol optical depth (DAOD), concentration, and deposition. Our results in Section 3 suggest that most models overestimate the contribution of African dust to the global dust cycle, while they underestimate the contribution of Asian dust. As discussed in Section 4, our data set can be used both to improve global dust cycle simulations and to constrain dust impacts on the Earth system, including on regional and global climate, weather, air quality, ecosystems, and the hydrological cycle.

2 Methods

We seek to constrain the contributions of the world's major source regions to the global dust cycle. We do so by analyzing constraints obtained in our companion paper (Kok et al., in review) on the dust loading, concentration, emission flux, wet and dry deposition fluxes, and DAOD generated by each source region. These constraints were obtained through an analytical framework that used an inverse model to integrate an ensemble of model simulations with observational constraints on dust properties and abundance. Briefly, we used simulations from six different global models of dust emitted by each of nine major source regions (Fig. 1) and for each model particle bin (or mode) extending to a maximum diameter of 20 μm. We then used optimal estimation to determine how many units of dust loading from each source region and particle bin produces best agreement against observational constraints on the dust size distribution, extinction efficiency, and regional dust aerosol optical depth. This approach yielded constraints on the dust loading, optical depth, concentration, and emission and deposition fluxes that are resolved by location, season, and particle size. These constraints include uncertainties propagated from the spread in model simulation results and in the observationally informed constraints on dust microphysical properties and regional DAOD. The companion paper (Kok et al., in review) shows that this approach resulted in a representation of the Northern Hemisphere global dust cycle that is substantially more accurate than obtained from both a large number of climate and chemical transport model simulations and the MERRA-2 dust product (Buchard et al., 2017), with modest improvements for the Southern Hemisphere.

Below, we first describe how we used the results from this inverse model to obtain the fractional contribution to dust loading, concentration, emission flux, wet and dry deposition fluxes, and DAOD generated by each source region (Section 2.1). For the remainder of this paper, we refer to these results as the "inverse model" results. We then describe our analysis of the dust emission, dust loading, and DAOD generated by each source region in the ensemble of AeroCom Phase 1 global model simulations (Huneeus et al., 2011) (Section 2.2).
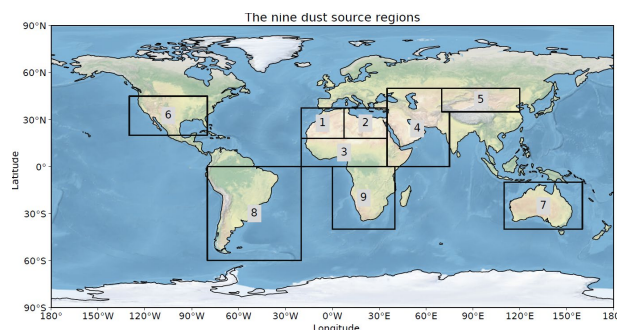
Figure 1. Coordinates of the nine main source regions used in this study. The nine source regions are: (1) western North Africa, (2) eastern North Africa, (3) Southern Sahara & Sahel, (4) Middle East & Central Asia (which includes the Horn of Africa), (5) East Asia, (6) North America, (7) Australia, (8) South America, and (9) Southern Africa. Exact coordinates for these regions are given in Kok et al. (in review). After Kok et al. (in review); made with Natural Earth.

2.1 Attribution of the global dust cycle to the different dust source regions

The analysis in Kok et al. (in review) integrated an ensemble of global model simulations with observational constraints on dust properties and abundance to obtain the size-resolved dust optical depth, column loading, emission flux, deposition flux,

130 and concentration for each season and source region. Here we used these inverse modeling results to constrain the fractional contribution of each source region to size-resolved DAOD ($\breve{f}_{\tau_{r,s,k}}$), column loading ($\breve{f}_{l_{r,s,k}}$), dust concentration ($\breve{f}_{C_{r,s,k}}$), and dust deposition flux ($\breve{f}_{D_{r,s,k}}$). These fields are a function of longitude (θ), latitude (ϕ), pressure level (P; in the case of dust concentration), and season (subscript s) and are obtained for different particle size bins (subscript k) spanning $0.2 - 0.5$, $0.5 - 1.0$, $1.0 - 2.5$, $2.5 - 5.0$, $5.0 - 10$, and $10 - 20$ μm (see Kok et al. (in review) for the exact methodology). That is,

$$\breve{f}_{\tau_{r,s,k}}(\theta,\phi) = \breve{\tau}_{r,s,k}(\theta,\phi) / \sum_{r=1}^{N_{sreg}} \breve{\tau}_{r,s,k}(\theta,\phi), \tag{1}$$

$$\breve{f}_{l_{r,s,k}}(\theta,\phi) = \breve{l}_{r,s,k}(\theta,\phi) / \sum_{r=1}^{N_{sreg}} \breve{l}_{r,s,k}(\theta,\phi), \tag{2}$$

$$\breve{f}_{C_{r,s,k}}(\theta,\phi,P) = \breve{C}_{r,s,k}(\theta,\phi,P) / \sum_{r=1}^{N_{sreg}} \breve{C}_{r,s,k}(\theta,\phi,P), \tag{3}$$

$$\breve{f}_{D_{r,s,k}}(\theta,\phi) = \breve{D}_{r,s,k}(\theta,\phi) / \sum_{r=1}^{N_{sreg}} \breve{D}_{r,s,k}(\theta,\phi), \tag{4}$$

135 where $\breve{\tau}_{r,s,k}(\theta,\phi)$, $\breve{l}_{r,s,k}(\theta,\phi)$, $\breve{C}_{r,s,k}(\theta,\phi,P)$, and $\breve{D}_{r,s,k}(\theta,\phi)$ are the contributions of each source region r to respectively the DAOD, loading, concentration, and total (dry and wet) deposition flux in season s for particle bin k. Similarly, the fractional contributions of each source region to bulk DAOD ($\breve{f}_{\tau_{r,s}}$), dust column loading ($\breve{f}_{l_{r,s}}$), dust concentration ($\breve{f}_{C_{r,s}}$), and dust deposition flux ($\breve{f}_{D_{r,s}}$) are

$$\breve{f}_{\tau_{r,s}}(\theta,\phi) = \breve{\tau}_{r,s}(\theta,\phi) / \sum_{r=1}^{N_{sreg}} \breve{\tau}_{r,s}(\theta,\phi), \tag{5}$$

$$\breve{f}_{l_{r,s}}(\theta,\phi) = \breve{l}_{r,s}(\theta,\phi) / \sum_{r=1}^{N_{sreg}} \breve{l}_{r,s}(\theta,\phi), \tag{6}$$

$$\breve{f}_{C_{r,s}}(\theta,\phi,P) = \breve{C}_{r,s}(\theta,\phi,P) / \sum_{r=1}^{N_{sreg}} \breve{C}_{r,s}(\theta,\phi,P), \tag{7}$$

$$\breve{f}_{D_{r,s}}(\theta,\phi) = \breve{D}_{r,s}(\theta,\phi) / \sum_{r=1}^{N_{sreg}} \breve{D}_{r,s}(\theta,\phi), \tag{8}$$

where $\breve{\tau}_{r,s}(\theta,\phi)$, $\breve{l}_{r,s}(\theta,\phi)$, $\breve{C}_{r,s}(\theta,\phi,P)$, and $\breve{D}_{r,s}(\theta,\phi)$ are respectively the bulk DAOD, dust loading, concentration, and

140 total (wet and dry) deposition flux generated by dust from source season r in season s, obtained from the analysis in Kok et al. (in review).

The DAOD, column loading, concentration, and deposition fields used in Eqs. (1)-(8) are probability distributions that account for the propagation of errors in the observational constraints and modeling results that were used as inputs to generate these

145   fields (see section 2.5 in Kok et al., in review). The fractional contribution of each source region to DAOD, column loading,

concentration, and deposition flux obtained by Eqs. (1)-(8) are thus also probability distributions. We added the mean and

median, the upper and lower one standard error estimates, and the upper and lower two standard error estimates to the Dust

Constraints from joint Experimental-Modeling-Observational Analysis (DustCOMM) dataset (Adebiyi et al., 2020), which is

available at https://dustcomm.atmos.ucla.edu/.

150   **2.2 Obtaining emission, loading, and DAOD per source region from AeroCom models**

As described in more detail in the companion paper (Kok et al., in review), we analyzed 13 AeroCom Phase I simulations of

the dust cycle in the year 2000 (Huneeus et al., 2011) for comparison against our inverse model's results of the contribution

of each source region to the global dust cycle. Since AeroCom simulations did not track the source region of atmospheric dust

after emission, we used our ensemble of model simulations (see Table 1 in Kok et al., in review) to estimate regional differences

155   in the conversion of source-specific dust emission to source-specific global loading, and the conversion of source-specific

global loading to source-specific global DAOD. Specifically, we estimated the global loading (Tg) generated by dust emitted

from source region r as simulated by an AeroCom model as:

$$\tilde{L}_r^{\text{Aer}} = \tilde{F}_r^{\text{Aer}} \tilde{T}_{\text{glob}}^{\text{Aer}} \frac{\breve{T}_r}{\breve{T}_{\text{glob}}}, \tag{9}$$

where $\tilde{F}_r^{\text{Aer}}$ is the bulk emission flux generated by source region r simulated by a given AeroCom model, $\tilde{T}_{\text{glob}}^{\text{Aer}}$ is the global

bulk (mass-weighted) dust lifetime simulated by the AeroCom model (obtained from Table 3 in Huneeus et al. (2011)), and

160    $\breve{T}_r$ and $\breve{T}_{\text{glob}}$ are respectively the mean bulk lifetimes for source region r and for dust from all source regions (both obtained

from our analysis, see Fig. 3a below). As such, $\breve{T}_r/\breve{T}_{\text{glob}}$ estimates the ratio of the lifetime of dust from source region r to the

global dust lifetime. This ratio is used in Eq. (9) to correct the global dust lifetime simulated by an AeroCom model to the

lifetime for dust emitted from source region r, which in turn is used to calculate the dust loading generated by source region r

from its emission flux.

165

We furthermore obtain the DAOD generated by the dust emitted from source region r as simulated by an AeroCom model as:

$$\tilde{\tau}_r^{\text{Aer}} = \frac{\tilde{L}_r^{\text{Aer}}}{A_{\text{Earth}}} \breve{\epsilon}_{\text{glob}}^{\text{Aer}} \frac{\breve{\epsilon}_r}{\breve{\epsilon}_{\text{glob}}}, \tag{10}$$

where A_{Earth} is the Earth's surface area (m²) and $\breve{\epsilon}_{\text{glob}}^{\text{Aer}}$ is the bulk dust mass extinction efficiency (MEE) simulated by a given

AeroCom model (obtained from Table 3 in Huneeus et al. (2011)). Similar to the approach used in Eq. (9), $\breve{\epsilon}_r$ and $\breve{\epsilon}_{\text{glob}}$ are

respectively the bulk dust MEE for source region r and for dust from all source regions (both also obtained from our analysis,

170   see Table 3 in Kok et al. (in review)).

3. Results

We report each source region's contributions to the global dust cycle on annual and seasonal timescales in Sections 3.1 and 3.2, respectively. We then report the spatial distribution of dust column loading and DAOD in Section 3.3 and the spatial distribution of dust deposition fluxes in Section 3.4.

3.1 Constraints on each source region's contribution to the global dust cycle

We obtained each source region's absolute and fractional contributions to the global dust emission and deposition flux, the global dust loading, and the global DAOD (see Table 1 and Figs. 2g-i). For comparison, we also obtained these properties for our ensemble of simulations (Figs. 2d-f) and for the AeroCom Phase I model ensemble (see Section 2.2, Table 1, and Figs. 2a-c).

Our results on each source region's contribution to the global dust cycle show some notable differences from our model ensemble and the AeroCom Phase I ensemble. First, our inverse model results indicate that PM_{20} dust emission fluxes for all source regions are substantially greater than most models include (Table 1; also see Kok et al., in review). This is in part because many models simulate dust up to a maximum geometric diameter smaller than 20 μm (see further discussion in Kok et al., in review) and in part because most models that do simulate dust with diameter larger than 10 μm substantially underestimate dust emission and loading in the 10-20 μm diameter range (Adebiyi and Kok, 2020; Huang et al., 2020). Accounting for this additional coarse dust in the atmosphere is important because it produces a substantial direct radiative forcing (Ryder et al., 2019; Adebiyi and Kok, 2020) and because it accounts for a large fraction of dust deposition fluxes to marine and terrestrial ecosystems (see below).

A second important difference between our results and that of the two model ensembles is in the fractional contributions per source region to the global dust cycle. Both multi-model ensemble means show that ~60-65% of dust loading and DAOD is generated by North African source regions, ~20-25% from the Middle East & Central Asia, ~7-9% from East Asia, <1% from North America, and ~5% from the Southern Hemisphere source regions (Figs. 2a-c). In contrast, we find that North African dust contributes only about half of the global dust loading (one standard error range of 11-15 Tg) and DAOD (0.012-0.023). Specifically, we find that the Southern Sahara & Sahel source region contributes about ~15% of global dust loading (with a large one standard error range of 1.5-5.7 Tg), and that western North Africa (~20%; 3.9-6.8 Tg) likely contributes substantially more dust than Eastern North Africa (~15%; 1.8-5.6 Tg). These fractional contributions of western and eastern North Africa are substantially less than the average for models in our ensemble and in the AeroCom ensemble, both of which obtained a ~25-30% contribution for both regions. These findings that most models overestimate the fractional contribution of North Africa to global dust loading and that western North Africa generates a larger dust loading than eastern North Africa appear to be consistent with satellite observations (Engelstaedter et al., 2006; Shindell et al., 2013). We further find that the Southern Sahara & Sahel contributes ~15% of the global dust and ~30% of North African dust. Models in our ensemble find a similar fractional contribution from the Southern Sahara & Sahel but models in the AeroCom ensemble simulated a contribution of

205 on average only ~6%, thereby possibly underestimating the contribution from the Southern Sahara & Sahel by about a factor of two. Our finding of a larger contribution to global dust loading from the Southern Sahara & Sahel is consistent with the fact that this source region includes the Bodélé Depression, which is a major dust source (Warren et al., 2007). Nonetheless, our results add to an emerging consensus (Glaser et al., 2015; Bozlaker et al., 2018; Yu et al., 2020) that dust from the Bodélé Depression accounts for much less than the previously-proposed ~half of North African dust transported across the Atlantic

210 (Koren et al., 2006; Washington et al., 2009; Evan et al., 2015).
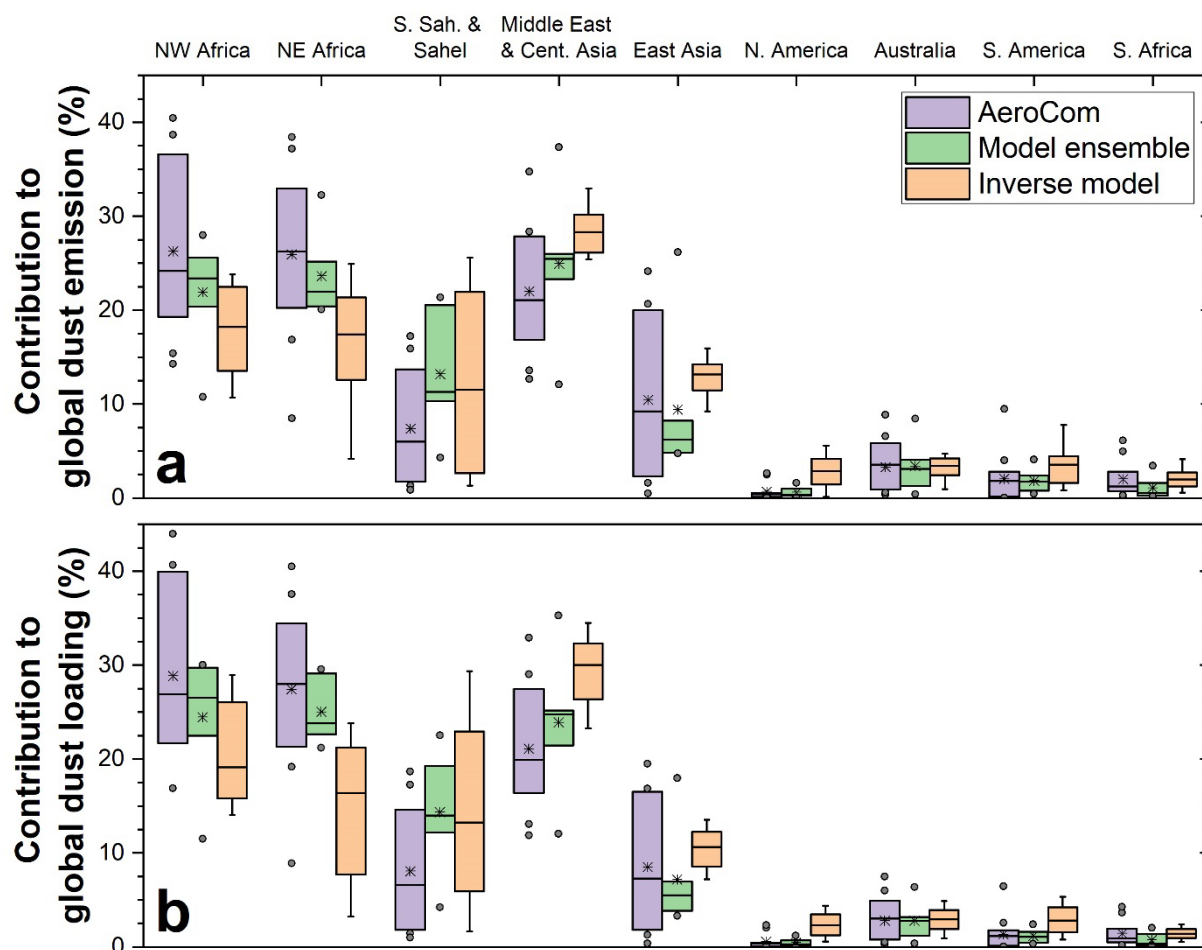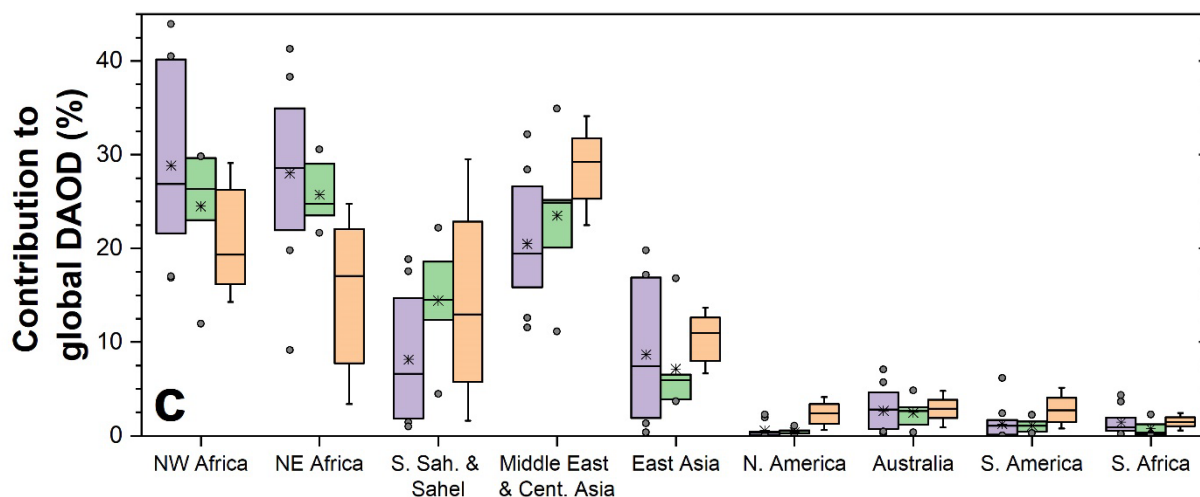
215

Figure 2. Fractional contribution of each source region to the global dust cycle. Shown are the fractional contributions to the annual global dust emission (and deposition) flux (**a**)**,** the global dust loading (**b**), and the global DAOD (**c**) for the AeroCom ensemble (purple boxes; see Section 2.2) our model ensemble (green boxes) and for the inverse model (orange boxes). Box boundaries approximately denote the one standard error range (i.e., boxes contain 9 out of 13 AeroCom simulations, 4 out of 6 model ensemble members, and the 68%

220 probability range for the inverse model's results), gray circles denote the individual simulation results outside of this range, whiskers denote the 95% confidence interval for the inverse model results, horizontal solid lines denote the median result, and stars denote the mean result. Results for each season are shown in Figs. S1-S4.

After the North African source regions, we find that Asian source regions account for the bulk of the remainder of global dust

225 emissions, loading, and DAOD. In particular, the Middle Eastern and Central Asian source regions account for ~30% of global dust loading (6.1-9.4 Tg), which is more than the ~20-25% estimated from the AeroCom ensemble and our model ensemble. We further find that East Asian source regions account for another ~11% of global dust loading (2.0-3.4 Tg), which is more than the ~7% estimated from the two model ensembles. Overall, we find that Asian dust accounts for ~40% of global dust loading.

230

Table 1. Contributions of the world's nine major source regions to the global dust cycle. Listed are median values for the AeroCom Phase I ensemble and the inverse model's results, with one standard error intervals listed in parentheses. For the AeroCom ensemble, the one standard range was obtained from the range spanned by the 9 central model results out of the 13 total model results, which corresponds to the central 69% of model results. For the inverse model results, the one error range was obtained from the central 68% of results from a

235 large number (10^3) bootstrap iterations (see Kok et al., in review). Note that inverse model results are for dust with $D \leq 20$ μm, whereas the size range accounted for by AeroCom models differs for each model (see Huneeus et al. (2011)).

Source region	Annual dust emission and deposition rate ($\times 10^3$ Tg/year)		Percentage of annual dust emission and deposition		Dust loading (Tg)		Percentage of dust loading		Dust AOD ($\times 10^3$)		Percentage of dust AOD		Mass extinction efficiency (m²/g)	
	Aero-Com	Inverse model	Aero-Com	Inverse model	Aero-Com	Inverse model	Aero-Com	Inverse model	Aero-Com	Inverse model	Aero-Com	Inverse model	Aero-Com	Inverse model
All source regions	1.7 (1.2-3.1)	4.7 (3.4-9.1)	100 (99-100)*	100 (99-100)*	20 (14-23)	26 (22-30)	100 (99-100)	100 (99-100)	30 (21-35)	27 (24-30)	100 (99-100)	100 (99-100)	0.69 (0.60-0.96)	0.54 (0.47-0.62)
All of North Africa	1.0 (0.5-1.7)	2.1 (1.6-4.3)	60 (55-69)	46 (44-49)	12 (8-18)	13 (11-15)	66 (59-74)	50 (47-55)	20 (13-22)	14 (13-15)	66 (60-74)	50 (48-55)	0.69 (0.61-0.97)	0.55 (0.48-0.63)
All of the Southern Hemisphere	0.10 (0.03-0.20)	0.47 (0.30-0.78)	6 (2-11)	9 (7-12)	0.9 (0.3-1.5)	1.8 (1.3-2.4)	5 (1-8)	7 (5-9)	1 (0-2)	2 (1-2)	5 (1-8)	7 (5-9)	0.65 (0.57-0.93)	0.53 (0.47-0.61)
Western North Africa	0.41 (0.28-0.60)	0.88 (0.64-1.44)	24 (19-37)	18 (14-22)	5.0 (3.3-6.2)	5.2 (3.8-6.9)	27 (22-40)	19 (16-26)	7.4 (5.2-11.1)	5.6 (4.2-7.1)	27 (22-40)	19 (16-26)	0.68 (0.60-0.97)	0.55 (0.48-0.63)
Eastern North Africa	0.44 (0.27-0.82)	0.72 (0.47-1.11)	26 (20-33)	16 (7-21)	5.3 (3.8-8.2)	4.3 (2.0-5.5)	28 (21-34)	16 (8-21)	8.1 (6.0-10.5)	4.8 (2.2-6.0)	29 (22-35)	17 (8-22)	0.70 (0.62-0.99)	0.56 (0.49-0.64)
Southern Sahara & Sahel	0.10 (0.03-0.29)	0.56 (0.15-1.77)	6 (2-14)	13 (4-20)	1.4 (0.4-2.1)	3.5 (1.5-5.6)	7 (2-15)	14 (6-22)	2.1 (0.5-2.7)	3.8 (1.6-5.4)	7 (2-15)	13 (6-22)	0.69 (0.61-0.98)	0.53 (0.46-0.61)
Middle East / Central Asia	0.34 (0.19-0.56)	1.38 (0.97-2.59)	21 (17-28)	29 (27-32)	4.5 (1.8-5.7)	7.7 (6.0-9.3)	20 (16-27)	30 (26-32)	4.9 (4.0-8.0)	8.0 (6.4-9.1)	19 (16-27)	29 (25-32)	0.66 (0.59-0.94)	0.52 (0.46-0.60)
East Asia	0.18 (0.02-0.31)	0.58 (0.42-1.12)	9 (2-20)	13 (10-15)	1.8 (0.2-2.7)	2.7 (2.0-3.4)	7 (2-17)	11 (9-12)	2.1 (0.4-5.9)	3.0 (2.0-3.6)	7 (2-17)	11 (8-13)	0.70 (0.62-0.99)	0.53 (0.46-0.63)
North America	0.01 (0.00-0.01)	0.13 (0.05-0.24)	0 (0-1)	3 (1-4)	0.1 (0.0-0.1)	0.6 (0.3-0.9)	0 (0-0)	2 (1-3)	0.1 (0.0-0.1)	0.6 (0.4-0.9)	0 (0-0)	2 (1-3)	0.67 (0.59-0.94)	0.54 (0.46-0.64)
Australia	0.04 (0.01-0.09)	0.16 (0.09-0.29)	4 (1-6)	3 (2-5)	0.3 (0.1-0.9)	0.8 (0.5-1.1)	3 (1-5)	3 (2-4)	0.4 (0.2-1.1)	0.8 (0.5-1.1)	3 (1-5)	3 (2-4)	0.64 (0.57-0.91)	0.53 (0.46-0.61)
South America	0.02 (0.00-0.07)	0.19 (0.10-0.35)	2 (0-3)	4 (2-6)	0.1 (0.0-0.5)	0.7 (0.4-1.1)	1 (0-2)	3 (2-4)	0.1 (0.0-0.5)	0.7 (0.4-1.1)	1 (0-2)	3 (2-4)	0.65 (0.57-0.91)	0.52 (0.45-0.60)
Southern Africa	0.02 (0.01-0.05)	0.10 (0.06-0.19)	1 (1-3)	2 (1-3)	0.2 (0.1-0.4)	0.4 (0.2-0.5)	1 (1-2)	1 (1-2)	0.4 (0.1-0.5)	0.4 (0.3-0.5)	1 (1-2)	1 (1-2)	0.69 (0.61-0.97)	0.57 (0.50-0.66)

240 *The fraction of global emissions of desert dust accounted for by the nine source regions is calculated by using simulated global emissions in the latitude band of 50S – 50N. This was done to exclude high latitude dust emissions, which the inverse model does not account for.

We find that the lesser source regions of North and South America, Australia, and South Africa account for ~10% of the global dust loading (1.8-3.2 Tg). This is substantially more than the ~5-6% of the global dust loading that both model ensembles estimate for these minor source regions. In particular, we find that the relative contribution of North America to global dust

245 loading is ~2.5% (0.3-0.9 Tg), or ~5 times greater than estimated by both model ensembles (see further discussion in Section 3.4.1). Similarly, the relative contribution of South America is approximately twice as large (~3% of global dust loading (0.4-

1.1 Tg). However, there are large uncertainties in our estimates for these minor source regions because it is difficult to obtain accurate constraints on the DAOD over those regions. In particular, the contributions of other aerosol species (e.g., sea spray) to total AOD can be larger than that due to dust (Ridley et al., 2016), which propagates into large uncertainties for our constraint

250   on dust emissions, loading, and DAOD generated by these source regions (see Table 1). Nonetheless, our results further confirm that the global dust cycle is dominated by Northern Hemisphere dust, with Southern Hemisphere dust accounting for less than 10% of global dust loading.

The moderate differences between each source region's fractional contribution to global dust loading and emission/deposition

255   fluxes (Fig. 2) are due to differences in the lifetimes of dust from each source region (Fig. 3). We find that atmospheric lifetimes are largest for dust emitted from the world's main source regions in North Africa and the Middle East & Central Asia. As discussed in more detail in Section 3.2, this likely occurs because dust emitted from these regions experiences strong convection, lofting the dust to greater heights in the atmosphere (Cakmur et al., 2004). The relatively large lifetime of North African dust causes it to account for half (~50%) of the global dust loading and DAOD, even though it accounts for somewhat

260   less than half (~46%) of the global PM_{20} dust emissions (Fig. 2 and Table 1). Differences in size-resolved lifetimes (Figure S5) also drive small differences in the MEE between the different source regions (Table 1; note that we do not account for regional differences in MEE due to differences in dust mineralogy (Perlwitz et al., 2015a; Scanza et al., 2015)).
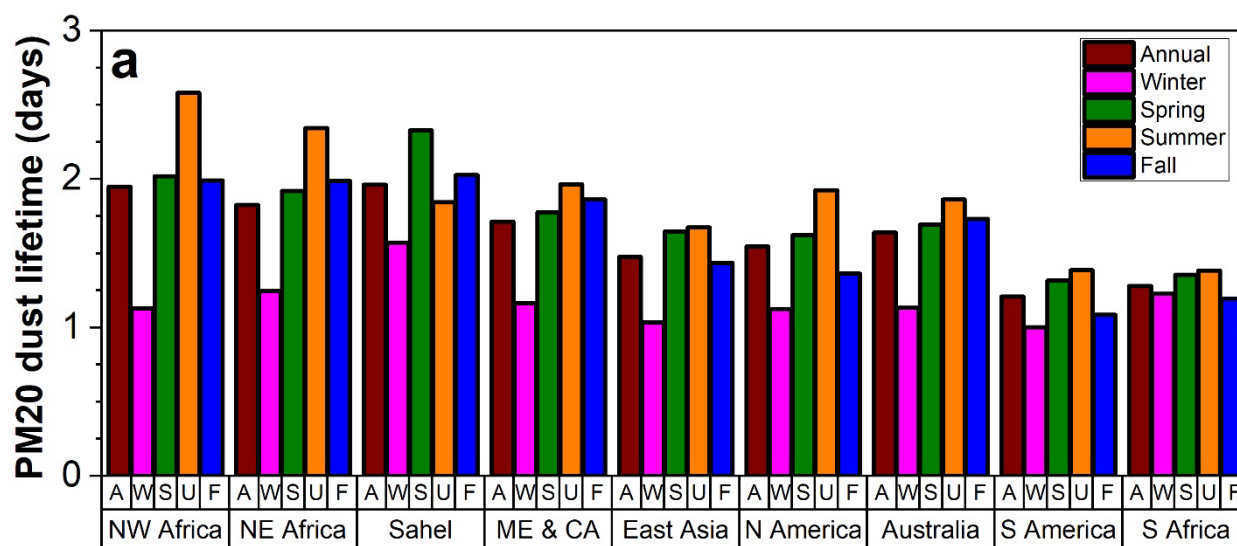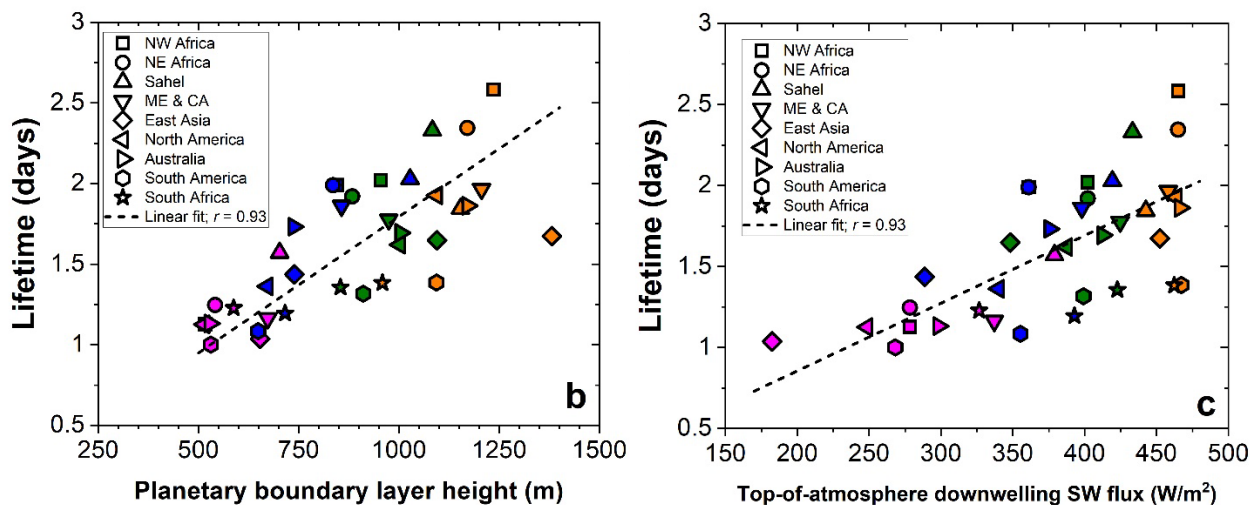
Figure 3. Seasonal variation of dust lifetime for the different source regions. (**a**) Mass-weighted lifetime of PM$_{20}$ dust for each source region on an annual basis (A; brown bars) and for each source region's local winter (W), spring (S), summer (U), and fall (F) seasons (magenta, green, orange, and blue bars). Variations in dust lifetime are largely explained by differences in downwelling SW flux (panel **b**) and planetary boundary layer (PBL) height (panel **c**). This indicates that the increase is modeled dust lifetime in spring and summer is due to increased convection, which lofts dust to greater altitudes. Colors of symbols in panels **b** and **c** denote the season per the color scheme in panel **a**. The TOA downwelling SW flux was obtained from Wong and Chow (2001), the seasonally averaged PBL height was obtained from the GISS Model E2.1 simulation (Kelley et al., 2020), and the mass-weighted dust lifetimes were obtained from the ratio of the PM$_{20}$ dust loading with the deposition flux for each source region and season. Size-resolved annual and seasonal dust lifetimes are shown in Figs. S5 – S9.

3.2 Seasonality of each source region's dust cycle

We further analyzed our results to obtain the seasonality of each source region's dust cycle (Fig. 4). We find that only ~15-30% of the total PM$_{20}$ deposition flux is due to wet deposition, with some variability with season and source region. This dominance of deposition fluxes by dry deposition in all seasons occurs because coarse dust dominates the total emission flux and those particles are predominantly removed through dry deposition (e.g., Miller et al., 2006). However, most of this dry deposition flux is due to coarse dust depositing close to source regions, and wet deposition remains dominant further from source regions (Yu et al., 2019; van der Does et al., 2020). All source regions show peaks in dust loading and DAOD in spring or summer, and these seasons are substantially dustier than the fall and winter seasons for both the Northern and the Southern Hemispheres. Our results are consistent with well-known features of the seasonality of the dust cycle, such as spring/summer-time peaks in Saharan dust loading, spring-time peaks in Sahelian and East Asian dust loading, and spring/summer-time peaks in Australian dust loading (Goudie and Middleton, 2001; Prospero et al., 2002; Ekstrom et al., 2004; Ginoux et al., 2012; Knippertz and Todd, 2012; Xu et al., 2016).

We find that an important contributor to the peaks in dustiness in spring and summer is an enhanced dust lifetime during those

290   seasons (Fig. 3). A correlation analysis shows that, on average, approximately one third of the seasonal variation in dust loading

is due to the seasonal variability in lifetime, with the rest explained by seasonal variability in emissions. In fact, several source

regions do not show a clear peak in emissions during spring and summer (i.e., western and eastern North Africa and Southern

Africa), but nonetheless show clear peaks in loading and DAOD that are driven by the increased lifetime in those seasons. This

seasonality in the lifetime is likely driven by the stronger convection in spring and summer, lofting emitted dust to greater

295   heights in those seasons when solar insolation is largest. One exception might be the Sahel, for which the lifetime in Fall is

longer than in Summer (Fig. 3a), which appears to be due to increased wet deposition (Fig. 4f), presumably due to proximity

to the Intertropical Convergence Zone and the West African monsoon in summer (Glaser et al., 2015). Nonetheless, we find

that most of the variance in dust lifetime between seasons and source regions is explained by differences in the planetary

boundary layer depth ($R^2 = 0.86$; Fig. 3b), which in turn are largely due to differences in the top-of-atmosphere shortwave

300   downwelling flux ($R^2 = 0.86$; Fig. 3c).
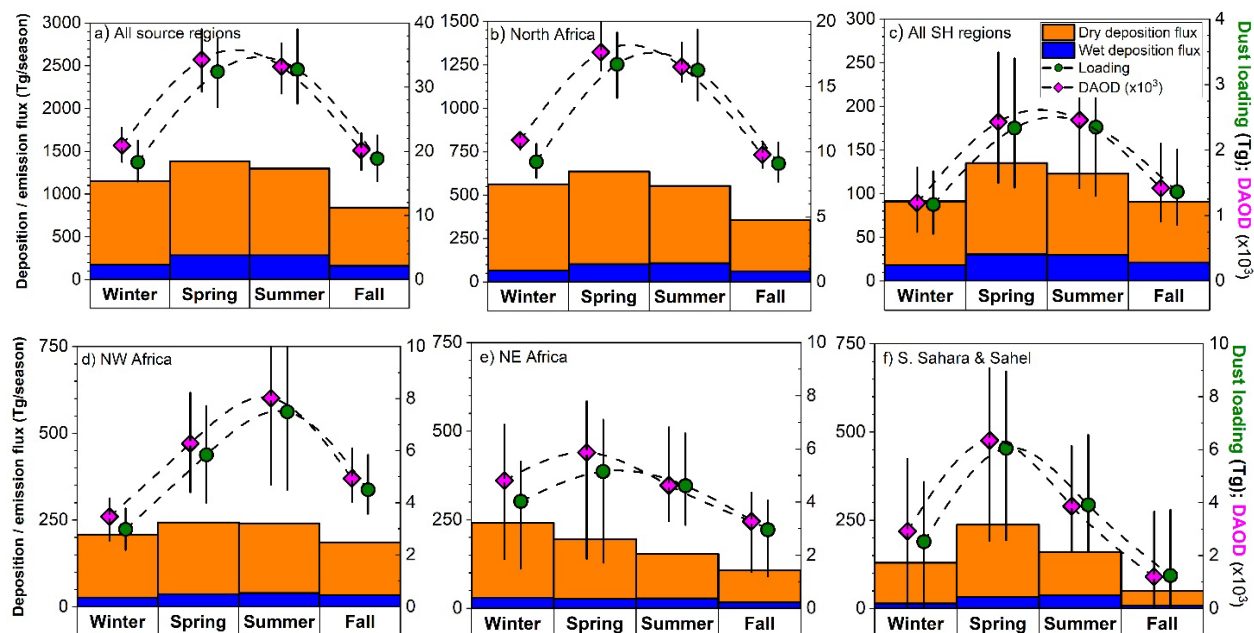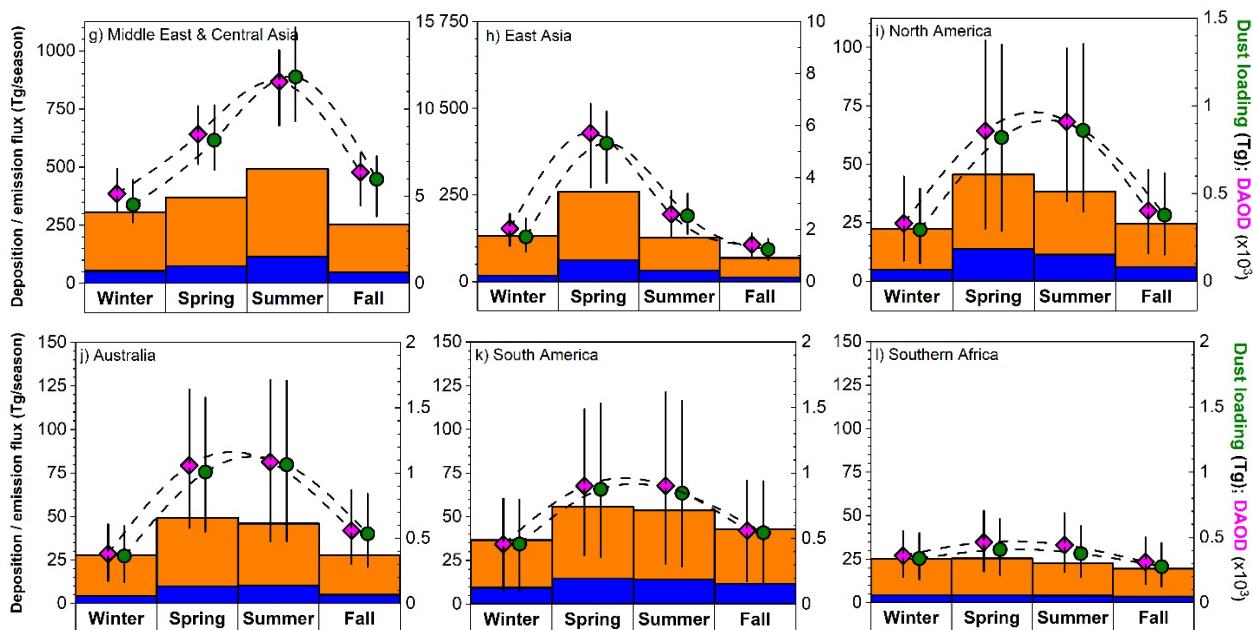
Figure 4. Seasonal contributions of each source region to the global dust cycle. Shown are the seasonal cycles of the wet deposition flux (blue bars and left axis), dry deposition flux (brown bars and left axis), dust loading (green circles and right axis), and DAOD (magenta diamonds and right axis) generated by (**a**) all source regions, (**b**) all North African source regions, (**c**) all Southern Hemisphere source regions, and (**d-l**) each of the nine individual source regions. The sum of the seasonal wet and dry deposition fluxes is approximately equal (within a few percent) to the seasonal dust emission flux generated by each source region. Results for loading and DAOD are slightly offset horizontally for clarity. Seasons refer to boreal seasons for global results (panel (**a**)) and for local seasons for all other panels. Note that the vertical axis scale differs between source regions. Error bars denote one standard error from the median; error bars on deposition fluxes usually exceeded 100% and are not included for clarity.

3.3 Spatial distribution of each source region's contribution to DAOD, column loading, and concentration

Consistent with the ~50% fractional contribution of North African source regions to the global DAOD, we find that North African dust contributes substantially to DAOD and loading in large fractions of the Northern Hemisphere, with dust from East Asia and the Middle East & Central Asia also contributing substantially in several regions (Figs. 5 and S11). However, the intertropical convergence zone (ITCZ) poses a formidable barrier to the inter-hemispheric transport of dust from these major Northern Hemisphere source regions (also see seasonal DAOD and loading results in Figures S12-S19). Even though Northern Hemisphere dust accounts for ~93% of the global dust loading, it contributes only up to ~10% to the dust loading south of the ITCZ. Note that this result depends sensitively on the ability of models to represent interhemispheric transport. Although other modeling studies have found somewhat different contributions of Northern Hemisphere source regions to Southern Hemisphere dust (e.g., Li et al., 2008; Albani et al., 2012), our results support the conclusion that dust in the Southern Hemisphere is overwhelmingly supplied by the Australian, South American, and South African source regions.
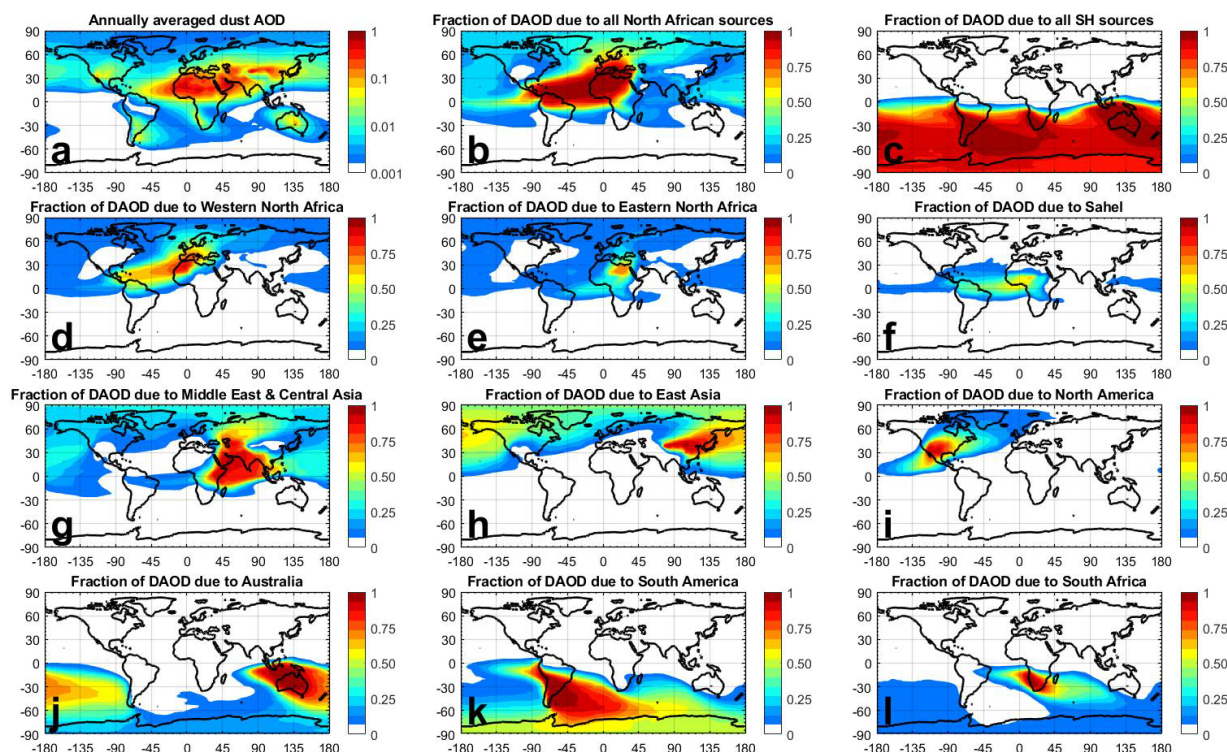
Figure 5. Attribution of the annually averaged DAOD to the world's main dust source regions. Shown first is (**a**) the annually averaged DAOD produced from all source regions combined, followed by the fraction of DAOD that is due to (**b**) all North African and (**c**) all Southern Hemisphere source regions. The fraction of DAOD due to each of the three North African source regions are shown in panels (**d**)-(**f**), and the fraction of DAOD due to the other three Northern Hemisphere source regions of Middle East & Central Asia, East Asia, and North America are shown in panels (**g**)-(**i**). Finally, the fraction of DAOD due to the three Southern Hemisphere source regions of Australia, South America, and South Africa are shown in panels (**j**)-(**l**). Attributions of seasonal DAOD to the different source regions are shown in Figures S12-S15.

Constraints on the zonally averaged dust concentration provide further insight into the contribution of the different source regions throughout the three-dimensional (3D) atmosphere (Fig. 6). We find that the interhemispheric transport of Northern Hemisphere (NH) dust is likely facilitated by strong vertical transport shown by dust emitted from the arid North African and Asian deserts (Fig. 6d-h), which probably plays a role in the longer lifetimes of dust emitted from those regions (Fig. 3). Consequently, the cross-equatorial transport of dust originating from the NH makes the largest fractional contribution to concentration in the SH stratosphere (<200 hPa; Fig. 6d-h), although transport into this region could be distorted by model errors in the middle atmosphere circulation that result from insufficient vertical resolution and an artificially low upper boundary (e.g., Rind et al., 2020). In the SH upper troposphere, dust originates mainly from austral sources (Fig. 6c). Although dust concentrations are small at this altitude (Fig. 6a), dust there could be critical for the heterogeneous nucleation of cirrus (Cziczo et al., 2013) and mixed-phase clouds (Vergara-Temprado et al., 2018), which could have important impacts on climate

345 (Storelvmo, 2017). Our results further indicate that transport of dust from the Southern to the Northern Hemisphere is less efficient than from the Northern to the Southern Hemisphere (Figs. 6c, j, k, l). Likely reasons for this include that SH dust has a lower average lifetime than NH dust (Fig. 3) and is emitted further from the equator and the summer ITCZ than dust from for instance North Africa and the Middle East.

350 It is important to note that the inverse model's vertical distribution of dust is largely determined by that simulated by the models in our ensemble as we have not incorporated observational constraints on dust vertical profiles. Since comparisons of model simulations against data from the Cloud-Aerosol Lidar with Orthogonal Polarization (CALIOP) and the Cloud–Aerosol Transport System (CATS) airborne lidars indicate substantial discrepancies (Yu et al., 2010; Kim et al., 2014; Koffi et al., 2016; O'Sullivan et al., 2020), results presented here likely suffer from similar biases. A future version of this product could
355 thus use dust extinction profiles retrieved from CALIOP (Omar et al., 2010) and CATS (Yorks et al., 2014) to constrain the vertical distribution of dust.
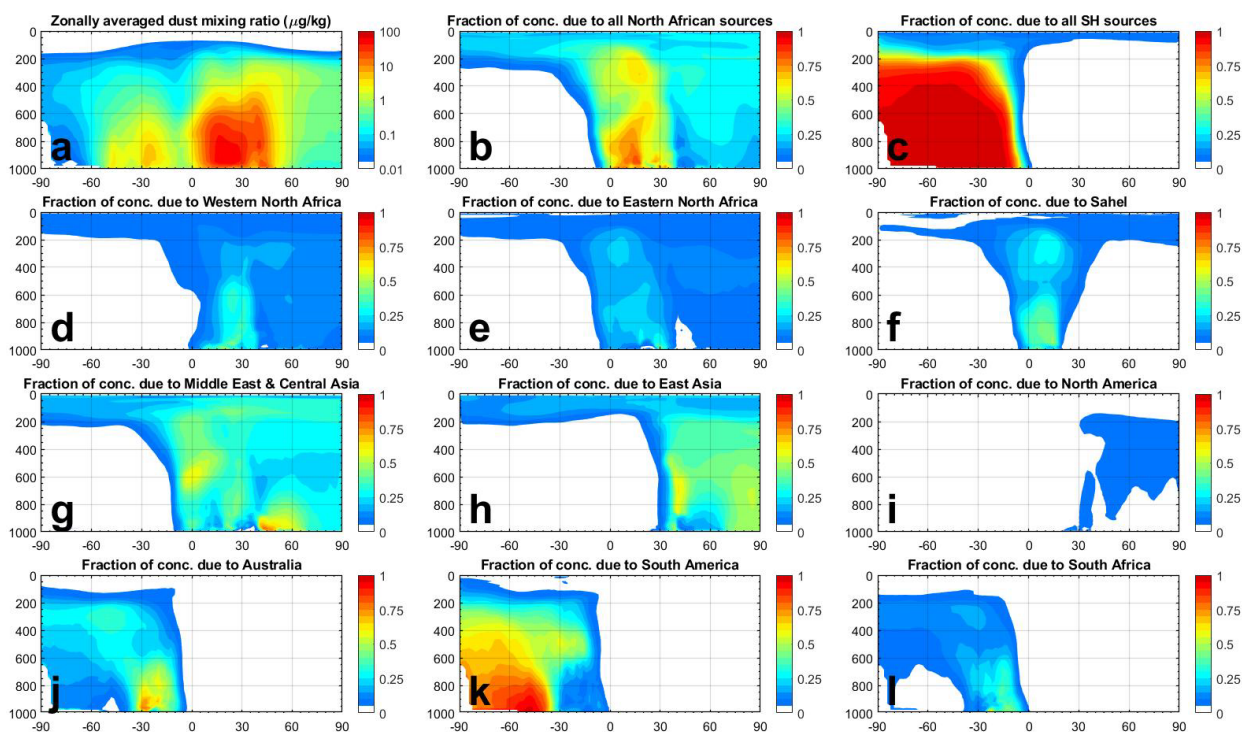
Figure 6. Attribution of the zonally averaged and annually averaged PM$_{20}$ dust concentration to the world's main source regions.
360 Panel (a) shows the zonally averaged dust mixing ratio (dust concentration normalized by air density) as a function of latitude (horizontal axis) and pressure in hPa (vertical axis). Panels (b)-(l) show the partition of the dust concentration per source region, with panel ordering identical to Figure 5. The seasonally resolved attribution of the zonally averaged dust concentration is shown in Figures S20-S23.

3.4 Constraints on each source region's contribution to dust deposition fluxes

365   We used our results to attribute the dust deposition flux to the different major source regions (Figs. 7 and 8a). These results strongly mirror the attribution of dust loading and DAOD. For instance, North African dust accounts for ~20-100% of dust deposition in much of the Northern Hemisphere (Fig. 7b). Dust from East Asia and the Middle East & Central Asia account for the bulk of the remaining dust deposition and dominate in large regions near their respective source regions (Figs. 7g, 7h, 8a). We also find that Northern Hemisphere dust contributes only a few percent of dust deposition fluxes throughout most of

370   the Southern Hemisphere (Fig. 7c; Tables 2 and 3).
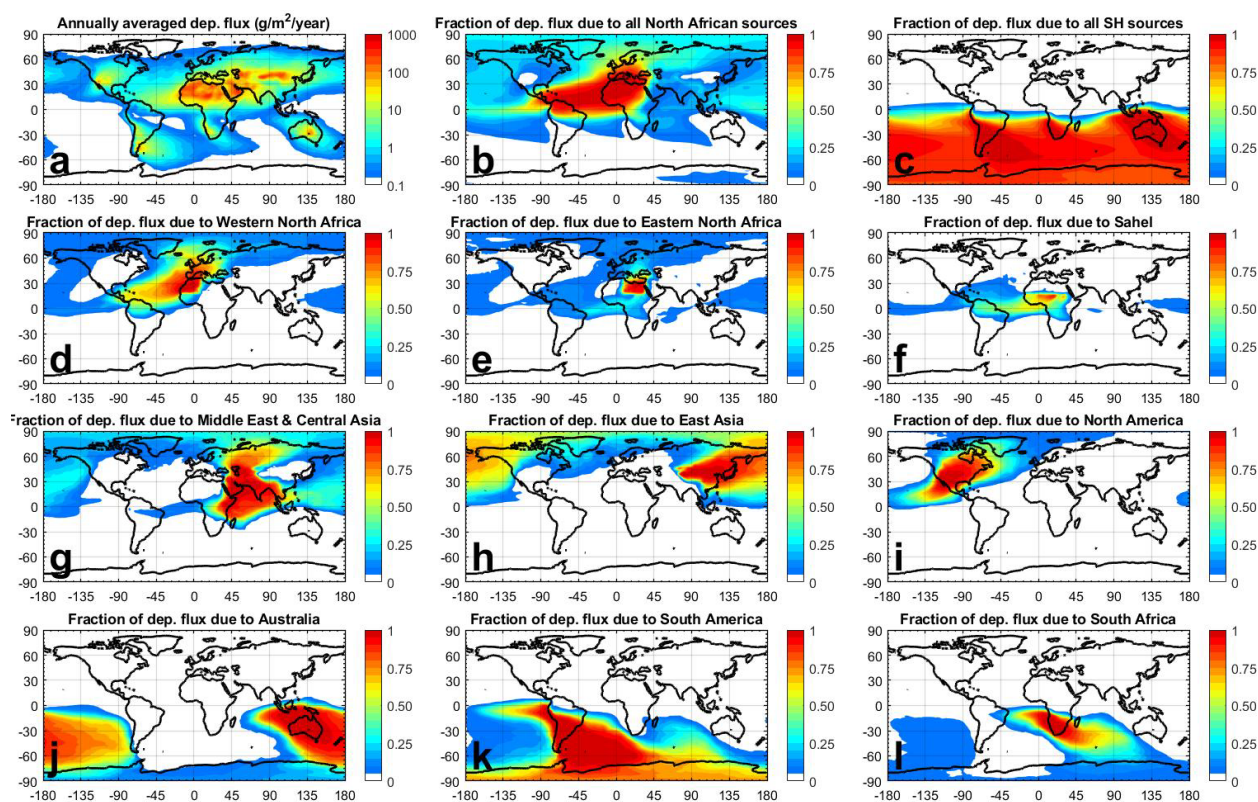
Figure 7. Attribution of the annually averaged deposition flux of PM$_{20}$ dust to the world's main source regions. Panel ordering is identical to Figure 5 and the seasonally resolved attribution of the dust deposition flux is shown in Figures S25-
375   28.
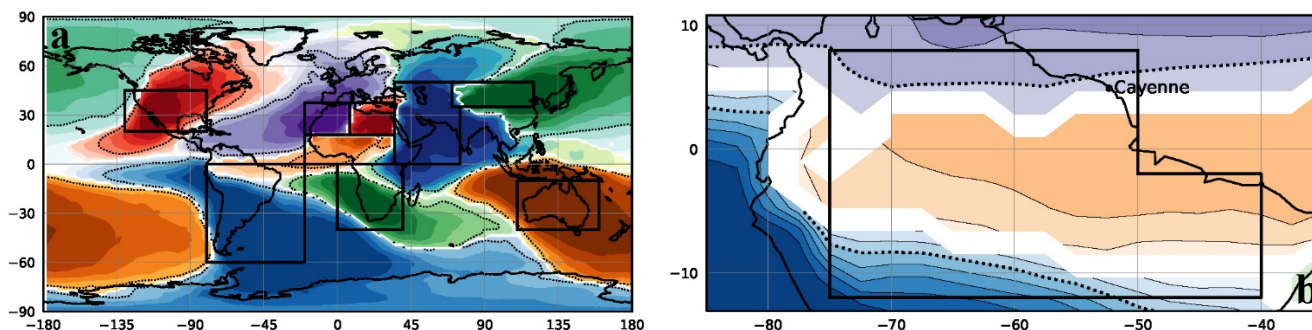
Figure 8. Percentage of dust deposition supplied by the dominant source region at each location for (a) the entire globe and (b) the Amazon rainforest. Different colors represent different dominant source regions, with shading decreasing in 10% increments from a maximum of 100% to a minimum of 20%. The 50% contour is identified by a black dotted line and white shading denotes areas where two or more dust source regions contribute similarly to the deposition flux. The black boxes in panel (a) denote the nine major source regions, and the black box in panel (b) denotes the boundaries of the Amazon rainforest used here, based on Yu et al. (2015). Also shown in (b) is Cayenne, the location of the field site where Prospero et al. (2020) obtained dust measurements (see text).

3.4.1 Dust deposition to high albedo regions

We also constrained the deposition fluxes to land regions for which dust deposition produces important impacts (Table 2). This includes the snow and ice-covered regions of Antarctica, the Arctic, and the Tibetan plateau (Lee et al., 2017; Kylling et al., 2018; Sarangi et al., 2020). Dust deposition to these high albedo regions can darken snow and icepacks, thereby producing warming and accelerating melting (Painter et al., 2010; Shao et al., 2011; Mahowald et al., 2014; Skiles et al., 2018). We find that the Tibetan plateau, being adjacent to major East Asian source regions (e.g., the Taklimakan Desert), receives a large deposition flux of 16 (11-25) Tg/year. This is consistent with findings that snowpack darkening from increasing dust deposition has played an important role in the regional warming of this region (Lau et al., 2010; Sarangi et al., 2020).

Greenland receives a relatively smaller dust deposition flux of 0.19 (0.07-0.52) Tg that is supplied by several different source regions, namely Northern Africa (30 (19-45) %), East Asia (26 (14-32) %), and North America (26 (11-50) %). (Note that we constrain deposition of desert dust only, and thus do not include deposition of dust from high latitude sources supplied by glacial sediments, which is likely an important contributor at the coastal margins of Greenland (Bory et al., 2003; Bullard et al., 2016).) Our finding that North American dust contributes substantially to dust deposited to Greenland (Figs. 7i, 8a) seems to disagree with geochemical data, which thus far has not identified a clear contribution from North American dust (Bory et al., 2003). This suggests that our results might overestimate North American dust emission, which is approximately a factor of five larger than predicted by most models in both the AeroCom phase I ensemble and in our own model ensemble (Fig. 2

and Table 1). This overestimation would most likely be due to an overestimate of the DAOD over North America that we used to constrain regional emission (Kok et al., in review). This regional DAOD was obtained from an ensemble of aerosol reanalysis products (Adebiyi et al., 2020), which might thus overestimate DAOD over North America. Furthermore, the inverse

405 model finding of roughly equal contributions of the East Asian and North African source regions to dust deposition to Greenland is in mixed agreement with geochemical data. These data indicate that East Asia is the main source of dust deposited to several ice core sites in the interior of Greenland (Bory et al., 2002; Bory et al., 2003), with dust from North Africa probably contributing as a secondary source (Lupker et al., 2010). This possible disagreement between the inverse model results and geochemical data is noteworthy, as the inverse model shows a substantially greater contribution from East Asian dust and a

410 smaller contribution from North African dust than most models in both model ensembles (see Fig. 2 and Table 1). As such, the underestimation of Asian dust and overestimation of African dust relative to results from geochemical studies would be larger for models in the two ensembles than for the inverse model. This finding suggests that current models either substantially underestimate transport of East Asian dust or overestimate transport of North African dust to Greenland.

415 **Table 2. Constraints on the contribution of dust deposition from each source region to land areas where dust deposition produces important impacts, namely the high albedo regions of Antarctica, Greenland, and the Tibetan Plateau, and the Amazon rainforest.** Listed are median values, with one standard error intervals listed in parentheses. The coordinates of the Amazon rainforest follow the definition given in Yu et al. (2015), and the Tibetan plateau was taken as the region with elevation over 4000m between 26-40N and 75-105E, based on Easter et al. (2004). These regions are plotted in Fig. S24.

Source region:	Antarctica	Greenland	Tibetan plateau	Amazon rainforest	All land regions
Total deposition from all source regions (Tg/year)	0.14 (0.03-0.55)	0.19 (0.07-0.52)	16 (11-25)	8.5 (2.9-9.7)	3.8 (2.7-7.5) × 10³
Percentage from:					
North African source regions	0 (0-1)	30 (19-45)	4 (2-6)	90 (86-94)	47 (45-50)
Southern Hemisphere source regions	99 (98-100)	0 (0-5)	0 (0-0)	6 (4-12)	7 (5-8)
Western North Africa	0 (0-0)	18 (13-32)	1 (1-2)	41 (28-53)	19 (14-22)
Eastern North Africa	0 (0-0)	6 (4-12)	2 (0-3)	11 (6-24)	17 (7-22)
S. Sahara & Sahel	0 (0-1)	3 (1-5)	1 (0-1)	36 (16-53)	13 (5-22)
Middle East & Central Asia	0 (0-1)	11 (7-19)	18 (14-30)	2 (2-3)	29 (26-32)
East Asia	0 (0-0)	26 (14-32)	77 (67-82)	0 (0-0)	14 (11-17)
North America	0 (0-0)	26 (11-50)	0 (0-0)	0 (0-0)	3 (1-4)
Australia	18 (6-36)	0 (0-1)	0 (0-0)	0 (0-0)	3 (2-4)

South America	71 (50-90)	0 (0-2)	0 (0-0)	5 (2-11)	2 (1-3)
South Africa	8 (3-13)	0 (0-2)	0 (0-0)	1 (0-2)	1 (1-2)

420

We also quantified each source region's contribution to dust deposited to Antarctica. We find that the total dust deposition flux to Antarctica equals 0.14 (0.03-0.55) Tg, of which South America provides the bulk (~70%) of the deposited dust, with smaller contributions from Australia (~20%) and South Africa (~10%), and almost no contribution from NH dust (Fig. 7 and

425 Table 2). As such, South America is the dominant dust source region for almost the entire continent of Antarctica (Fig. 8a). These findings are in good agreement with ice core records, for which geochemical fingerprinting has indicated that most present-day deposited dust originates from South America, with a smaller contribution from Australia (Mosley-Thompson et al., 1990; Souney et al., 2002; McConnell et al., 2007; Delmonte et al., 2008; Bory et al., 2010; Delmonte et al., 2019).

3.4.2 Dust deposition to the Amazon rainforest

430 We also obtained the dust deposition flux to the Amazon rainforest, for which the productivity on timescales of decades to millennia is partially controlled by delivery of phosphorus by settling dust (Swap et al., 1992; Okin et al., 2004). We find that the Amazon rainforest receives an average annual dust flux of 0.9 (0.3-1.1) g m^{-2} year^{-1}, which corresponds to a total annual dust deposition flux of 8.5 (2.9-9.7) Tg/year (Table 3). This is similar to results from the (unmodified) simulations in our ensemble, which predict a median Amazon deposition flux of 11.0 Tg and a range of 4.4 to 14.8 Tg. Further, our results are

435 quantitatively similar to the Amazon dust deposition flux of 8 – 10 Tg/year obtained by Prospero et al. (2020) based on dust measurement at Cayenne (French Guiana) and the dust product of the Modern-Era Retrospective analysis for Research and Applications, Version 2 (Buchard et al., 2017; Randles et al., 2017). Note that these results might somewhat underestimate deposition fluxes because most current models are unable to simulate the long-range transport of super-coarse dust with $D >$ 10 μm (Ansmann et al., 2017; Weinzierl et al., 2017).

440

The Amazon deposition fluxes found here (for the years 2004-2008) and in Prospero et al. (2020) are a factor of ~2-3 less than the 28 (8-50) Tg/year obtained from an analysis of 2007-2013 data from the CALIOP satellite instrument by Yu et al. (2015). Our lower estimate of dust deposition for the Amazon rainforest is expected because the CALIOP study substantially underestimated the dust extinction efficiency far from source regions. Indeed, the CALIOP estimates used a mass extinction

445 efficiency (MEE) of 0.37 m^2/g after Kaufman et al. (2005), which is less than the globally integrated mass extinction efficiencies of ~0.68 and ~0.54 m^2/g predicted by AeroCom models and obtained here (Table 1), respectively. Furthermore, the MEE for dust near the Amazon rainforest is larger than the globally integrated MEE (Figure S10) because most coarse particles deposit during long-range transport across the Atlantic. Indeed, the recent DustCOMM dataset (Adebiyi et al., 2020), which explicitly accounts for the enhancement of dust extinction due to particle asphericity, shows an MEE of ~0.8 – 1.0 m^2/g

450 after trans-Atlantic transport of North African dust. This is in good agreement with available measurements (Li et al., 1996;

Denjean et al., 2016; Figs. 8 and 9 in Adebiyi et al., 2020). We similarly find that the MEE over the Amazon rainforest is 0.86 (0.76-1.05) m²/g, such that the CALIOP-derived results likely underestimate the MEE by a factor of ~2-3, thereby overestimating deposition fluxes by the same factor. Taking this bias in the assumed MEE into account would bring the CALIOP-derived deposition fluxes in agreement with our results. These results emphasize the need for accurate and spatially-

455 varying constraints on the MEE, such as provided here and in Adebiyi et al. (2020) as part of the DustCOMM dataset. Overall, our results add to a growing consensus that, although the dust-borne delivery of phosphorus is likely critical for the long-term productivity of the Amazon rainforest, these fluxes are substantially less than previously thought and are rivaled by the delivery of more soluble phosphorus by biomass burning aerosols from Southern Africa (Barkley et al., 2019; Prospero et al., 2020).

460 Our finding of a substantially lower deposition flux to the Amazon rainforest illustrates the advantages of integrating observational, experimental, and modeling constraints. Results from analyses of model simulations and satellite data are subject to possibly substantial biases due to a number of required assumptions, including regarding the optical properties and size distribution of dust. In our approach, dust properties are instead based on observational constraints for which the uncertainties have been propagated into our results (Kok et al., 2017; Adebiyi and Kok, 2020), and for which quantitative

465 predictions can be evaluated against independent measurements (see Kok et al., in review). In addition, our approach integrates a variety of regional measurements ranging from AOD to dust size distributions along with model estimates of transport, in contrast to observational estimates of nutrient supply based upon a more limited range of observations or retrievals. Two further advantages of the constraints presented here are that they are source region-resolved and are available globally. This former factor is particularly important for accounting for the effects of regional differences in soil mineralogy on dust impacts

470 on radiation (Perlwitz et al., 2015a; Scanza et al., 2015), clouds (Atkinson et al., 2013; Shi and Liu, 2019), and biogeochemistry (Zhang et al., 2015), as well as for interpreting records of dust deposition from natural archives (Albani et al., 2015).

Our results also provide insight into the source regions that provide dust to the Amazon rainforest (Fig. 8b). Previous studies have argued that either the Bodélé depression (Koren et al., 2006) or El Djouf (Yu et al., 2020) are dominant contributors to

475 dust deposition to the Amazon. However, we find that the western North Africa source region (containing El Djouf) and the Southern Sahara & Sahel source region (containing the Bodélé depression) contribute roughly equally to the Amazonian dust deposition flux. Indeed, western North Africa contributes 41 (28-53) % and dominates the deposition flux in the northern part of the Amazon rainforest, whereas the Southern Sahara & Sahel contributes 36 (16-53) % and dominates in the central and Eastern parts of the Amazon rainforest. The contribution of both the western North Africa and Southern Sahara & Sahel source

480 regions peak in boreal Spring, with smaller contributions in Winter and Summer (Figs. S25-S28). Most of the remainder of the dust deposition flux is supplied by eastern North African dust (11 (6-24) %) and notably by South American dust (5 (2-11) %), which dominates in the southwestern part of the Amazon. Overall, our results thus indicate that a large number of different source regions make important contributions to dust deposition to the Amazon rainforest.

3.4.3 Dust deposition to oceanic regions

485 We further used our results to quantitatively constrain the PM_{20} dust deposition flux of each source region to each ocean basin (Table 3). Dust deposition provides critical nutrients, such as phosphorus and iron, to open ocean regions such as the Southern Ocean and the North Pacific where primary productivity can be limited by the supply of these dust-borne nutrients (Jickells et al., 2005; Myriokefalitakis et al., 2018). Consequently, glacial-interglacial variations in atmospheric dust deposition flux to the oceans are hypothesized to have modulated atmospheric CO_2 concentrations (Martin, 1990; Ridgwell and Watson, 2002;

490 Lambert et al., 2008). We constrain the total flux of PM_{20} dust deposited to oceans to be 0.8 (0.6-1.3) $\times$ 10^3 Tg. This is approximately double the median deposition flux to oceans that was obtained in recent model ensemble studies (Table 5 in Checa-Garcia et al., 2020; Tables 8 and 9 in Wu et al., 2020). This larger dust deposition flux to oceanic regions likely occurs because we correct the underestimation (or omission) by current models of dust with geometric diameters between 10 to 20 μm (Adebiyi and Kok, 2020), which we find makes up approximately half (46 (35-66) %) of this deposition flux to oceans.

495 Although the bulk of this dust deposition to oceans occurs in oceanic basins surrounding major source regions (Fig. 7a), especially for coarse dust, we also find significant fluxes into more remote nutrient-limited ocean basins, such as a deposition flux of 25 (6-51) Tg/year to the Southern Ocean (Table 2), much of which originates from South America.

Table 3. Constraints on the contribution of dust deposition from each source region to the world's main ocean basins. Listed are
500 median values, with one standard error intervals listed in parentheses. Coordinates of ocean basins are based on NOAA's World Ocean Atlas (Locarnini et al., 2010). All regions are plotted in Fig. S24 for clarity.

Source region:	South Atlantic Ocean	North Atlantic Ocean	South Pacific Ocean	North Pacific Ocean	Indian Ocean	Mediterranean Sea	Southern Ocean	Arctic Ocean	All ocean regions
Total deposition from all source regions (Tg/year)	86 (51-149)	229 (168-344)	19 (10-34)	74 (50-106)	189 (121-314)	57 (35-78)	25 (6-51)	2 (1-6)	0.8 (0.6-1.3) $\times 10^3$
Percentage from:									
North African source regions	4 (2-8)	95 (91-98)	1 (0-2)	8 (4-15)	5 (2-6)	99 (96-99)	0 (0-0)	28 (22-51)	38 (33-43)
Southern Hemisphere source regions	95 (91-97)	0 (0-1)	98 (97-100)	0 (0-2)	12 (5-17)	0 (0-1)	100 (99-100)	0 (0-1)	21 (15-27)
Western North Africa	0 (0-1)	58 (43-73)	0 (0-1)	3 (2-6)	1 (0-1)	36 (20-42)	0 (0-0)	17 (13-37)	21 (15-26)
Eastern North Africa	1 (0-4)	8 (2-17)	0 (0-1)	3 (1-6)	3 (1-4)	62 (55-75)	0 (0-0)	7 (4-13)	10 (3-13)
S. Sahara & Sahel	2 (1-5)	22 (9-44)	0 (0-1)	1 (1-3)	1 (0-1)	2 (1-3)	0 (0-0)	2 (1-4)	7 (3-15)
Middle East & Central Asia	1 (0-1)	2 (1-3)	0 (0-1)	10 (7-22)	83 (78-90)	1 (1-3)	0 (0-0)	23 (7-35)	31 (27-38)
East Asia	0 (0-0)	1 (0-1)	0 (0-0)	55 (41-76)	0 (0-1)	0 (0-0)	0 (0-0)	27 (21-33)	5 (3-9)

North America	0 (0-0)	2 (0-5)	0 (0-0)	14 (7-33)	0 (0-0)	0 (0-0)	0 (0-0)	15 (5-33)	3 (2-4)
Australia	0 (0-1)	0 (0-0)	68 (20-81)	0 (0-0)	7 (3-11)	0 (0-0)	10 (4-30)	0 (0-0)	3 (1-5)
South America	68 (28-84)	0 (0-1)	28 (15-78)	0 (0-1)	1 (0-2)	0 (0-0)	88 (63-94)	0 (0-0)	12 (6-18)
South Africa	24 (11-65)	0 (0-0)	2 (0-3)	0 (0-1)	3 (1-7)	0 (0-0)	2 (1-6)	0 (0-1)	5 (3-7)

4. Discussion

4.1 Limitations of the methodology

We consider the results presented in the previous section to be more accurate constraints on the source region-resolved dust
505 loading, concentration, DAOD, and deposition flux than results obtained directly from regional and global model simulations
(e.g., Tanaka and Chiba, 2006; Mahowald, 2007; Huneeus et al., 2011; Wu et al., 2020). Nonetheless, our results are subject
to a number of important limitations. Critically, the results obtained here depend on a number of previous products, including
the analytical framework to join observational and modeling constraints on the global dust cycle developed in our companion
paper (Kok et al., in review), the ensemble of climate and atmospheric chemistry model simulations, and constraints on the
510 globally averaged dust size distribution (Adebiyi and Kok, 2020) and the regional DAOD (Ridley et al., 2016). The results
presented here are therefore subject to the limitations of these studies, which are discussed in detail in the corresponding papers.

Some limitations from these previous studies are of particular relevance in the interpretation of our results. In particular, Ridley
et al. (2016) obtained the regional DAOD in dust-dominated regions by taking the total AOD - which was calculated from
515 satellite-retrieved AOD that was bias-corrected using ground-based aerosol optical depth measurements from the AErosol
RObotic NETwork (AERONET) – and subtracting the AOD from non-dust aerosol species simulated by an ensemble of four
model simulations. Although the error quantified by the spread in the model-simulated non-dust AOD for each region was
propagated into the results here, a systematic bias in model simulations of non-dust AOD would cause a systematic bias in the
regional DAOD in the Ridley et al. (2016) product. Such a bias could arise in particular for regions in which insufficient
520 observations are available to constrain models, and in which biomass burning and anthropogenic aerosols supply a large
fraction of AOD, as models rely on emission inventories to simulate those (Lamarque et al., 2010). Errors in emission
inventories would thus affect most or all models and cause a potentially substantial bias in the regional DAOD that is not
accounted for in our error analysis. Such a bias could in particular affect our constraints on Asian source regions, for which
there are also fewer in situ dust measurements available than for North African dust (e.g., Mahowald et al., 2009; Kok et al.,
525 in review). Furthermore, our constraints on the lesser source regions of North America, Australia, South America, and South
Africa rely on regional DAOD constraints obtained from an ensemble of aerosol reanalysis products (Adebiyi et al., 2020) that
assimilate ground- and satellite-based AOD retrievals. These products could similarly be biased because of difficulties
distinguishing dust from other aerosol species (see further discussion in Kok et al., in review). It is thus possible that some of

the differences between our results and model simulations, for instance the larger contribution of North American and Asian
530 sources found here than in model ensembles, could be due to such a bias in our results, model results, or both.

An additional limitation arises from possible systematic biases in dust transport simulated by the ensemble of models. If models
in our ensemble have consistent biases in representing dust transport from different source regions, then this would cause dust
from one source region to erroneously be assigned to another source region. For instance, if models systematically
535 underestimate the long-range transport of North African dust across East Asia and the North Pacific (Hsu et al., 2012), then
this could cause our results to overestimate the contribution of East Asian dust.

Finally, the climatology of the contributions of different source regions to the global dust cycle obtained here is based mostly
on model data and regional DAOD constraints for the period 2004-2008 (Ridley et al., 2016; Kok et al., in review). As such,
540 differences in the relative contributions of the main source regions before or after that period are not reflected in our results.

Although our methodology accounts for and propagates a large number of (quantifiable) errors in our analysis (Kok et al., in
review), the uncertainties on our results should thus be seen as lower bounds. The potential systematic biases described above
might cause actual errors to be substantially larger, especially for the Asian source regions (Middle East & Central Asia and
545 East Asia) and the lesser source regions (North America, Australia, South America, and South Africa). Note that (ensembles
of) model simulations are affected by these same issues. Indeed, although our errors likely underestimate the true errors, our
methodology mitigates model errors by drawing from an ensemble and by using constraints on dust abundance and dust
microphysical properties to correct model biases, resulting in substantially improved agreement against independent data (Kok
et al., in review). As such, our approach here, though subject to important limitations and biases, is likely to be more accurate
550 than (ensembles of) model simulations. Overall, these issues underscore the need to better constrain model simulations and
aerosol reanalysis products by obtaining more measurements of dust and other aerosol species outside of the regions affected
by North African dust and by obtaining more accurate constraints on speciated AOD (Kahn and Gaitley, 2015).

4.2 Implications for improving global dust cycle models and constraining dust impacts on the Earth system

Our constraints on each dust source region's size-resolved contribution to the global dust cycle can be used to constrain a
555 variety of important dust impacts on the Earth system. For instance, combining our results with spatially resolved and particle-
size resolved soil-surface mineralogy (Claquin et al., 1999; Journet et al., 2014) can help constrain the regionally-varying
mineralogy of dust aerosols (Kok, 2011; Perlwitz et al., 2015a; Scanza et al., 2015; Pérez Garcia-Pando et al., 2016; Li et al.,
2020). This has the potential to advance our understanding of a variety of important dust impacts that depend on mineralogy,
including dust impacts on the radiation budget (Scanza et al., 2015), on cirrus and mixed-phase clouds (Atkinson et al., 2013),
560 on atmospheric chemistry (Cwiertny et al., 2008), and on biogeochemical cycles (Mahowald, 2011; Ito et al., 2019; Hamilton
et al., 2020). Of particular note in this regard is the synergy with the data on surface mineralogy of dust source regions, such

as from the upcoming launch of the NASA Earth Surface Mineral Dust Source Investigation (EMIT) mission (Green et al., 2020).

565   A second important implication of our results is that our data can be used to inform the interpretation of dust deposition records from natural archives in the modern climate (Mahowald et al., 2010; Albani et al., 2012; Delmonte et al., 2013; Hooper and Marx, 2018). In particular, the constraints on the relative contribution of each source region to the deposition flux at measurement sites could inform the interpretation of changes in dust deposition fluxes through time.

570   Our results raise the question of why models produce a biased ranking of dust sources that need to be corrected by observationally informed constraints. Part of the cause of model biases is likely the limited knowledge of the emission environment. For instance, models may not correctly characterize the effects of topography, roughness, and vegetation that partially absorb the force of the wind and shield soil particles from erosion (King et al., 2005; Okin, 2008; Menut et al., 2013; Ito and Kok, 2017). Models also are limited by inadequate information on soil properties, such as soil size distribution and
575   aggregation state, and how those vary in space and time (Shao, 2001; Kok et al., 2014b). In addition, the relation between wind speed on the scale of the grid box and dust source is difficult to parameterize (Lunt and Valdes, 2002; Cakmur et al., 2004; Ridley et al., 2013; Comola et al., 2019), yet has a substantial effect because dust emissions are threshold dependent and scale non-linearly with wind speed (Shao, 2008; Kok et al., 2012). Furthermore, the mismatch between the wind speed at the resolved grid-box scale and that at the local dust source scale will vary regionally, partly as a result of sub-grid variations in topography.
580   For instance, the gap between the Tibesti and Ennedi mountains upwind of the Bodélé Depression is below the resolution of many global dust models but enhances the wind over the dust source compared to a grid-box average: a strengthening that is endemic and does not extend to most other grid boxes. Furthermore, models do not correctly capture some of the mesoscale meteorological events that might play an important role in the dust cycle (Schepanski et al., 2009), including haboobs (Pantillon et al., 2015) and possibly dust devils (Koch and Renno, 2005; Jemmett-Smith et al., 2015; Klose and Shao, 2016). Finally, one
585   other key reason for the difference between model simulations and the contributions of different source regions to the global dust cycle obtained here could be that models simulate mostly natural dust and commonly omit or underestimate anthropogenic dust such as from agricultural sources and fugitive dust, whereas the results obtained here inherently account for mineral dust from all natural and anthropogenic sources (see Kok et al., in review). As such, differences between our results and model results could also be due to the contribution of anthropogenic (agricultural and fugitive) dust, which could be substantial (Tegen
590   et al., 2004; Ginoux et al., 2012).

The results obtained here can address these weaknesses of models in accurately simulating emissions per source region by allowing models to tune each source region's dust cycle to match our observationally informed constraints. One approach is for models to scale their emissions such that a multi-year simulation, ideally over the period 2004-2008 to match the regional
595   DAOD constraints used in our inverse model (Ridley et al., 2016), matches our constraints on the size-resolved yearly emission

flux per source region. A preferable approach would be to scale model emissions to match either the loading or DAOD per source region to our constraints. This would be more difficult as the emission flux to generate a certain loading or DAOD depends on the model's simulated dust lifetimes, but this approach would be more accurate as it ties directly to our main observational constraint, namely on regional DAOD. Although these approaches could substantially improve simulations of

600   the present-day global dust cycle, it would be preferable to improve model physics such that such tuning is no longer necessary. This is particularly important for model predictions of interannual variability and of the global dust cycle for climates other than the present day. For instance, simulations of future changes in the global dust cycle diverge widely (Stanelle et al., 2014; Kok et al., 2018) and might be substantially biased (Evan et al., 2016). In this context, the accuracy of model upgrades to improve the accuracy of global dust cycle simulations could be verified through comparison against the observationally

605   informed constraints on dust emissions and loading per source region obtained here.

To facilitate the use of this paper's results in improving model simulations and constraining dust impacts on the Earth system, we report the emission flux, loading, DAOD, concentration, and (dry and wet) deposition fluxes that are generated by each of the nine source regions, resolved by location, season, and particle size. These data are publicly available as part of the

610   DustCOMM data set (Adebiyi and Kok, 2020; Adebiyi et al., 2020; Kok et al., in review), which is available at https://dustcomm.atmos.ucla.edu/. These data include uncertainties, which further increases its potential for improving constraints on the various dust impacts on the Earth system.

5. Conclusions

We have constrained the contribution of the world's main source regions to the global cycle of desert dust. We did so by

615   building on the improved representation of the global dust cycle that was obtained in the companion paper (Kok et al., in review). That work used an analytical framework with inverse modeling to integrate observational constraints on the properties and abundance of atmospheric dust with an ensemble of global model simulations. Here, we analyzed those inverse modeling results to constrain each source region's contribution to particle size-resolved dust loading, concentration, DAOD, and deposition flux.

620

We find that the global dust loading is partitioned as follows: North African dust contributes ~50%, including ~15% from the Southern Sahara & Sahel; Asian source regions contribute ~ 40%, with three quarters from the Middle East and Central Asia and one quarter from East Asia; and minor source regions contribute ~10%, with one quarter from North America and three quarters from the Southern Hemisphere source regions in Australia, South America, and South Africa (Fig. 2). Models in both

625   the AeroCom Phase I ensemble and in our model ensemble (Kok et al., in review) on average estimate a larger contribution of North African dust (~65%) and a smaller contribution of Asian dust (~30%) to atmospheric loading. These differences could be due to various factors (see Sections 4.1 and 4.2), including errors in representing dust emission and the relative contributions

of different source regions in models, biases in the regional DAOD used in our analytical framework, and the underestimation or omission of anthropogenic dust by models. We further find that Northern Hemisphere dust contributes only a small fraction

630 (<10%) to atmospheric loading and DAOD in the Southern Hemisphere (Figs. 5 and S11), but that this fraction increases with altitude and thus might be important for heterogeneous nucleation of ice crystals in mixed-phase and cirrus clouds (Shi and Liu, 2019). We further find that the deposition flux of dust to the Amazon basin is ~10 Tg, and thereby a factor of 2-3 less than obtained by previous work.

635 Our results indicate that dust loading in all source regions peaks in local spring or summer (Fig. 4). This is partially due to increased emissions for some source regions, and partially due to an increased dust lifetime in spring and summer for all source regions (Fig. 3a). In turn, this increased lifetime is likely caused by increased convection and thus increased boundary layer depth in the spring and summer seasons (Figs. 3b and c).

640 The dust source apportionment data sets obtained here are publicly available as part of the DustCOMM data set (Adebiyi et al., 2020) at http://dustcomm.atmos.ucla.edu. These data include the size-resolved contributions of each source region to dust emission and deposition fluxes, dust column loading, DAOD, and 3D dust concentration. All these gridded data sets are resolved by season and include uncertainties propagated from experimental and modeling uncertainties in the observational constraints on dust properties and abundance. As such, these data can be used to more accurately constrain the various dust

645 impacts of dust on the Earth system, and particularly those impacts that depend on particle size or the source-dependent dust mineralogy. This includes dust direct radiative effects and dust impacts on clouds, the hydrological cycle, and biogeochemical cycles.

Data availability

Data is available at https://dustcomm.atmos.ucla.edu/data/K21b/.

Author contributions

650 JFK designed the study, analyzed model data and wrote the manuscript. DSH, LL, NMM, and JSW performed CESM/CAM4 simulations; AI performed IMPACT simulations; RLM performed GISS ModelE2 simulations and produced Figure 8; PRC and ARL performed GEOS/GOCART simulations; MK, VO, and CPGP performed MONARCH simulations; and SA, YB and RCG performed INCA simulations. YH analyzed results from AeroCom Phase 1 models. AAA provided observational DAOD

655 constraints. MC and NMM provided valuable comments on study design. All authors edited and commented on the manuscript.

Competing interests

The authors declare that they have no conflict of interest.

Acknowledgements

This work was developed with support from the National Science Foundation (NSF) grants 1552519 and 1856389 awarded to
660 J.F.K, from the University of California President's Postdoctoral Fellowship awarded to A.A.A., from the European Union's
Horizon 2020 research and innovation programme under the Marie Skłodowska-Curie grant agreement No 708119 awarded
to S.A. and No. 789630 awarded to M.K. R. C.-G. received funding from the European Union's Horizon 2020 research
and innovation grant 641816 (CRESCENDO), and from JSPS KAKENHI Grant Number 20H04329 and Integrated Research
Program for Advancing Climate Models (TOUGOU) Grant Number JPMXD0717935715 from the Ministry of Education,
665 Culture, Sports, Science and Technology (MEXT), Japan to A.I. P.R.C. and A.R.-L. acknowledge support from the NASA
Atmospheric Composition: Modeling and Analysis Program (R. Eckman, program manager) and the NASA Center for Climate
Simulation (NCCS) for computational resources, Y.H. acknowledges NASA grant 80NSSC19K1346, awarded under the
Future Investigators in NASA Earth and Space Science and Technology (FINESST) program, and R.L.M. acknowledges
support from the NASA Modeling, Analysis and Prediction Program (NNG14HH42I). C.P.G.P. acknowledges support by the
670 European Research Council (grant no. 773051, FRAGMENT), the EU H2020 project FORCES (grant no. 821205), the AXA
Research Fund, and the Spanish Ministry of Science, Innovation and Universities (RYC-2015-18690 and CGL2017-88911-
R). M.K. and C.P.G.P. acknowledge PRACE for awarding access to MareNostrum at Barcelona Supercomputing Center to
run MONARCH. L.L. acknowledges support from the NASA EMIT project and the Earth Venture – Instrument program
(grant no. E678605). We also acknowledge high-performance computing support from Cheyenne (doi:10.5065/D6RX99HX)
675 provided by NCAR's Computational and Information Systems Laboratory, sponsored by the National Science Foundation. We
further thank Anna Benedictow for assistance in accessing the AeroCom modeling data, the AeroCom modeling groups for
making their simulations available.

References

Adebiyi, A.A., Kok, J.F., 2020. Climate models miss most of the coarse dust in the atmosphere. Science Advances 6,
680   eaaz9507.
Adebiyi, A.A., Kok, J.F., Wang, Y., Ito, A., Ridley, D.A., Nabat, P., Zhao, C., 2020. Dust Constraints from joint
    Observational-Modelling-experiMental analysis (DustCOMM): comparison with measurements and model simulations.
    Atmospheric Chemistry and Physics 20, 829-863.
Albani, S., Balkanski, Y., Mahowald, N., Winckler, G., Maggi, V., Delmonte, B., 2018. Aerosol-Climate Interactions During
685   the Last Glacial Maximum. Current Climate Change Reports 4, 99-114.
Albani, S., Mahowald, N.M., Delmonte, B., Maggi, V., Winckler, G., 2012. Comparing modeled and observed changes in
    mineral dust transport and deposition to Antarctica between the Last Glacial Maximum and current climates. Clim. Dyn.
    38, 1731-1755.

Albani, S., et al., 2014. Improved dust representation in the Community Atmosphere Model. J. Adv. Model. Earth Sy. 6, 541-570.

Albani, S., et al., 2015. Twelve thousand years of dust: the Holocene global dust cycle constrained by natural archives. Clim. Past. 11, 869-903.

Andreae, M.O., Jones, C.D., Cox, P.M., 2005. Strong present-day aerosol cooling implies a hot future. Nature 435, 1187-1190.

Ansmann, A., et al., 2017. Profiling of Saharan dust from the Caribbean to West Africa, Part 2: Shipborne lidar measurements versus forecasts. Atmospheric Chemistry and Physics Discussions.

Atkinson, J.D., et al., 2013. The importance of feldspar for ice nucleation by mineral dust in mixed-phase clouds. Nature 498, 355-358.

Balkanski, Y., Schulz, M., Claquin, T., Guibert, S., 2007. Reevaluation of Mineral aerosol radiative forcings suggests a better agreement with satellite and AERONET data. Atmos. Chem. Phys. 7, 81-95.

Barkley, A.E., et al., 2019. African biomass burning is a substantial source of phosphorus deposition to the Amazon, Tropical Atlantic Ocean, and Southern Ocean. Proc. Natl. Acad. Sci. U. S. A. 116, 16216-16221.

Biscaye, P.E., 1965. Mineralogy and sedimentation of recent deep-sea clay in atlantic ocean and adjacent seas and oceans. Geol. Soc. Am. Bull. 76, 803-&.

Bory, A., Wolff, E., Mulvaney, R., Jagoutz, E., Wegner, A., Ruth, U., Elderfield, H., 2010. Multiple sources supply eolian mineral dust to the Atlantic sector of coastal Antarctica: Evidence from recent snow layers at the top of Berkner Island ice sheet. Earth and Planetary Science Letters 291, 138-148.

Bory, A.J.M., Biscaye, P.E., Piotrowski, A.M., Steffensen, J.P., 2003. Regional variability of ice core dust composition and provenance in Greenland. Geochem. Geophys. Geosyst. 4.

Bory, A.J.M., Biscaye, P.E., Svensson, A., Grousset, F.E., 2002. Seasonal variability in the origin of recent atmospheric mineral dust at NorthGRIP, Greenland. Earth and Planetary Science Letters 196, 123-134.

Bozlaker, A., Prospero, J.M., Price, J., Chellam, S., 2018. Linking Barbados Mineral Dust Aerosols to North African Sources Using Elemental Composition and Radiogenic Sr, Nd, and Pb Isotope Signatures. Journal of Geophysical Research-Atmospheres 123, 1384-1400.

Buchard, V., et al., 2017. The MERRA-2 Aerosol Reanalysis, 1980 Onward. Part II: Evaluation and Case Studies. Journal of Climate 30, 6851-6872.

Bullard, J.E., et al., 2016. High-latitude dust in the Earth system. Reviews of Geophysics 54, 447-485.

Cakmur, R.V., Miller, R.L., Torres, O., 2004. Incorporating the effect of small-scale circulations upon dust emission in an atmospheric general circulation model. Journal of Geophysical Research-Atmospheres 109.

Checa-Garcia, R., et al., 2020. Evaluation of natural aerosols in CRESCENDO-ESMs: Mineral Dust. Atmos. Chem. Phys. Discuss. in review.

Chin, M., Diehl, T., Ginoux, P., Malm, W., 2007. Intercontinental transport of pollution and dust aerosols: implications for regional air quality. Atmospheric Chemistry and Physics 7, 5501-5517.

Claquin, T., Schulz, M., Balkanski, Y.J., 1999. Modeling the mineralogy of atmospheric dust sources. Journal of Geophysical Research-Atmospheres 104, 22243-22256.

Comola, F., Kok, J.F., Chamecki, M., Martin, R.L., 2019. The Intermittency of Wind-Driven Sand Transport. Geophysical Research Letters 46, 13430-13440.

Cwiertny, D.M., Young, M.A., Grassian, V.H., 2008. Chemistry and photochemistry of mineral dust aerosol. Annu. Rev. Phys. Chem. 59, 27-51.

Cziczo, D.J., et al., 2013. Clarifying the Dominant Sources and Mechanisms of Cirrus Cloud Formation. Science 340, 1320-1324.

Delmonte, B., Andersson, P.S., Hansson, M., Schoberg, H., Petit, J.R., Basile-Doelsch, I., Maggi, V., 2008. Aeolian dust in East Antarctica (EPICA-Dome C and Vostok): Provenance during glacial ages over the last 800 kyr. Geophysical Research Letters 35.

Delmonte, B., et al., 2013. Modern and Holocene aeolian dust variability from Tabs Dome (Northern Victoria Land) to the interior of the Antarctic ice sheet. Quat. Sci. Rev. 64, 76-89.

Delmonte, B., et al., 2019. Holocene dust in East Antarctica: Provenance and variability in time and space. Holocene.

Denjean, C., et al., 2016. Size distribution and optical properties of African mineral dust after intercontinental transport. Journal of Geophysical Research-Atmospheres 121, 7117-7138.

740 Di Biagio, C., et al., 2019. Complex refractive indices and single-scattering albedo of global dust aerosols in the shortwave spectrum and relationship to size and iron content. Atmospheric Chemistry and Physics 19, 15503-15531.

Di Biagio, C., et al., 2017. Global scale variability of the mineral dust long-wave refractive index: a new dataset of in situ measurements for climate modeling and remote sensing. Atmospheric Chemistry and Physics 17, 1901-1929.

Easter, R.C., et al., 2004. MIRAGE: Model description and evaluation of aerosols and trace gases. Journal of Geophysical
745 Research-Atmospheres 109.

Ekstrom, M., McTainsh, G.H., Chappell, A., 2004. Australian dust storms: Temporal trends and relationships with synoptic pressure distributions (1960-99). International Journal of Climatology 24, 1581-1599.

Engelstaedter, S., Tegen, I., Washington, R., 2006. North African dust emissions and transport. Earth-Sci. Rev. 79, 73-100.

Evan, A.T., Fiedler, S., Zhao, C., Menut, L., Schepanski, K., Flamant, C., Doherty, O., 2015. Derivation of an observation-
750 based map of North African dust emission. Aeolian Research 16, 153-162.

Evan, A.T., Flamant, C., Gaetani, M., Guichard, F., 2016. The past, present and future of African dust. Nature 531, 493-495.

Ginoux, P., Chin, M., Tegen, I., Prospero, J.M., Holben, B., Dubovik, O., Lin, S.J., 2001. Sources and distributions of dust aerosols simulated with the GOCART model. J. Geophys. Res. 106, 20255-20273.

Ginoux, P., Prospero, J.M., Gill, T.E., Hsu, N.C., Zhao, M., 2012. Global-scale attribution of anthropogenic and natural dust
755 sources and their emission rates based on MODIS Deep Blue aerosol products. Reviews of Geophysics 50, Rg3005.

Glaser, G., Wernli, H., Kerkweg, A., Teubler, F., 2015. The transatlantic dust transport from North Africa to the Americas-Its characteristics and source regions. Journal of Geophysical Research-Atmospheres 120, 11231-11252.

Goudie, A.S., Middleton, N.J., 2001. Saharan dust storms: nature and consequences. Earth-Sci. Rev. 56, 179-204.

Green, R.O., et al., 2020. The Earth Surface Mineral Dust Source Investigation: An Earth Science Imaging Spectroscopy
760 Mission, IEEE Aerospace Conference, Big Sky, MT, USA, pp. 1-15.

Grousset, F.E., Biscaye, P.E., 2005. Tracing dust sources and transport patterns using Sr, Nd and Pb isotopes. Chemical Geology 222, 149-167.

Hamilton, D.S., et al., 2020. Impact of Changes to the Atmospheric Soluble Iron Deposition Flux on Ocean Biogeochemical Cycles in the Anthropocene. Global Biogeochemical Cycles 34, 22.

765 Hooper, J., Marx, S., 2018. A global doubling of dust emissions during the Anthropocene? Glob. Planet. Change 169, 70-91.

Hsu, S.C., et al., 2012. Dust transport from non-East Asian sources to the North Pacific. Geophysical Research Letters 39.

Huang, J.P., Wang, T.H., Wang, W.C., Li, Z.Q., Yan, H.R., 2014. Climate effects of dust aerosols over East Asian arid and semiarid regions. Journal of Geophysical Research-Atmospheres 119, 11398-11416.

Huang, Y., Adebiyi, A.A., Kok, J.F., 2020. Linking the different diameter types of aspherical desert dust indicates that
770 models underestimate coarse dust emission, American Geophysical Union, Fall Meeting 2020, pp. abstract #A21I-2821.

Huneeus, N., et al., 2011. Global dust model intercomparison in AeroCom phase I. Atmos. Chem. Phys. 11, 7781-7816.

Ito, A., Kok, J.F., 2017. Do dust emissions from sparsely vegetated regions dominate atmospheric iron supply to the Southern Ocean? Journal of Geophysical Research-Atmospheres 122, 3987-4002.

Ito, A., et al., 2019. Pyrogenic iron: The missing link to high iron solubility in aerosols. Science Advances 5.

775 Ito, A., Ye, Y., Yamamoto, A., Watanabe, M., Aita, M.N., 2020. Responses of ocean biogeochemistry to atmospheric supply of lithogenic and pyrogenic iron-containing aerosols. Geological Magazine 157, 741-756.

Jemmett-Smith, B.C., Marsham, J.H., Knippertz, P., Gilkeson, C.A., 2015. Quantifying global dust devil occurrence from meteorological analyses. Geophysical Research Letters 42, 1275-1282.

Jickells, T.D., et al., 2005. Global iron connections between desert dust, ocean biogeochemistry, and climate. Science 308,
780 67-71.

Journet, E., Balkanski, Y., Harrison, S.P., 2014. A new data set of soil mineralogy for dust-cycle modeling. Atmospheric Chemistry and Physics 14, 3801-3816.

Journet, E., Desboeufs, K.V., Caquineau, S., Colin, J.L., 2008. Mineralogy as a critical factor of dust iron solubility. Geophysical Research Letters 35.

785 Kahn, R.A., Gaitley, B.J., 2015. An analysis of global aerosol type as retrieved by MISR. Journal of Geophysical Research-Atmospheres 120, 4248-4281.

Kaufman, Y.J., Koren, I., Remer, L.A., Tanre, D., Ginoux, P., Fan, S., 2005. Dust transport and deposition observed from the Terra-Moderate Resolution Imaging Spectroradiometer (MODIS) spacecraft over the Atlantic ocean. Journal of Geophysical Research-Atmospheres 110.

790 Kelley, M., et al., 2020. GISS-E2.1: Configurations and climatology. J. Adv. Model. Earth Syst. 12, e2019MS002025.

Kiehl, J.T., 2007. Twentieth century climate model response and climate sensitivity. Geophysical Research Letters 34.

Kim, D., et al., 2014. Sources, sinks, and transatlantic transport of North African dust aerosol: A multimodel analysis and comparison with remote sensing data. Journal of Geophysical Research-Atmospheres 119, 6259-6277.

King, J., Nickling, W.G., Gillies, J.A., 2005. Representation of vegetation and other nonerodible elements in aeolian shear
795 stress partitioning models for predicting transport threshold. Journal of Geophysical Research-Earth Surface 110.

Kinne, S., et al., 2006. An AeroCom initial assessment - optical properties in aerosol component modules of global models. Atmospheric Chemistry and Physics 6, 1815-1834.

Klose, M., Shao, Y.P., 2016. A numerical study on dust devils with implications to global dust budget estimates. Aeolian Research 22, 47-58.

800 Knippertz, P., Todd, M.C., 2012. Mineral dust aerosols over the sahara: Meteorological controls on emission and transport and implications for modeling. Reviews of Geophysics 50.

Koch, J., Renno, N.O., 2005. The role of convective plumes and vortices on the global aerosol budget. Geophysical Research Letters 32.

Koffi, B., et al., 2016. Evaluation of the aerosol vertical distribution in global aerosol models through comparison against
805 CALIOP measurements: AeroCom phase II results. Journal of Geophysical Research-Atmospheres 121, 7254-7283.

Kok, J.F., 2011. A scaling theory for the size distribution of emitted dust aerosols suggests climate models underestimate the size of the global dust cycle. Proc. Natl. Acad. Sci. U. S. A. 108, 1016-1021.

Kok, J.F., et al., in review. Improved representation of the global dust cycle using observational constraints on dust properties and abundance. Atmos. Chem. Phys.

810 Kok, J.F., Albani, S., Mahowald, N.M., Ward, D.S., 2014a. An improved dust emission model - Part 2: Evaluation in the Community Earth System Model, with implications for the use of dust source functions. Atmos. Chem. Phys. 14, 13043-13061.

Kok, J.F., et al., 2014b. An improved dust emission model - Part 1: Model description and comparison against measurements. Atmos. Chem. Phys. 14, 13023-13041.

815 Kok, J.F., Parteli, E.J.R., Michaels, T.I., Karam, D.B., 2012. The physics of wind-blown sand and dust. Rep. Prog. Phys. 75, 106901.

Kok, J.F., et al., 2017. Smaller desert dust cooling effect estimated from analysis of dust size and abundance. Nature Geoscience 10, 274-278.

Kok, J.F., Ward, D.S., Mahowald, N.M., Evan, A.T., 2018. Global and regional importance of the direct dust-climate
820 feedback. Nature Communications 9.

Koren, I., Kaufman, Y.J., Washington, R., Todd, M.C., Rudich, Y., Martins, J.V., Rosenfeld, D., 2006. The Bodele depression: a single spot in the Sahara that provides most of the mineral dust to the Amazon forest. Environmental Research Letters 1.

Kylling, A., Zwaaftink, C.D.G., Stohl, A., 2018. Mineral Dust Instantaneous Radiative Forcing in the Arctic. Geophysical
825 Research Letters 45, 4290-4298.

Lamarque, J.F., et al., 2010. Historical (1850-2000) gridded anthropogenic and biomass burning emissions of reactive gases and aerosols: methodology and application. Atmospheric Chemistry and Physics 10, 7017-7039.

Lambert, F., et al., 2008. Dust-climate couplings over the past 800,000 years from the EPICA Dome C ice core. Nature 452, 616-619.

830 Lau, W.K.M., Kim, M.K., Kim, K.M., Lee, W.S., 2010. Enhanced surface warming and accelerated snow melt in the Himalayas and Tibetan Plateau induced by absorbing aerosols. Environmental Research Letters 5, 10.

Lee, W.L., et al., 2017. Impact of absorbing aerosol deposition on snow albedo reduction over the southern Tibetan plateau based on satellite observations. Theoretical and Applied Climatology 129, 1373-1382.

Li, F., Ginoux, P., Ramaswamy, V., 2008. Distribution, transport, and deposition of mineral dust in the Southern Ocean and
835 Antarctica: Contribution of major sources. Journal of Geophysical Research-Atmospheres 113.

Li, L., et al., 2020. Quantifying the range of the dust direct radiative effect due to source mineralogy uncertainty Atmos. Chem. Phys. Discuss. in review.

Li, X., Maring, H., Savoie, D., Voss, K., Prospero, J.M., 1996. Dominance of mineral dust in aerosol light-scattering in the North Atlantic trade winds. Nature 380, 416-419.

840   Locarnini, R.A., et al., 2010. World Ocean Atlas

2009, Volume 1: Temperature, in: Levitus, S. (Ed.), NOAA Atlas NESDIS 68, p. 184.

Lunt, D.J., Valdes, P.J., 2002. The modern dust cycle: Comparison of model results with observations and study of sensitivities. Journal of Geophysical Research-Atmospheres 107.

Lupker, M., Aciego, S.M., Bourdon, B., Schwander, J., Stocker, T.F., 2010. Isotopic tracing (Sr, Nd, U and Hf) of
845   continental and marine aerosols in an 18th century section of the Dye-3 ice core (Greenland). Earth and Planetary Science Letters 295, 277-286.

Mahowald, N., 2011. Aerosol Indirect Effect on Biogeochemical Cycles and Climate. Science 334, 794-796.

Mahowald, N., Albani, S., Kok, J.F., Engelstaeder, S., Scanza, R., Ward, D.S., Flanner, M.G., 2014. The size distribution of desert dust aerosols and its impact on the Earth system. Aeolian Res. 15, 53-71.

850   Mahowald, N.M., 2007. Anthropocene changes in desert area: Sensitivity to climate model predictions. Geophysical Research Letters 34, L18817.

Mahowald, N.M., et al., 2009. Atmospheric Iron Deposition: Global Distribution, Variability, and Human Perturbations. Annual Review of Marine Science 1, 245-278.

Mahowald, N.M., et al., 2010. Observed 20th century desert dust variability: impact on climate and biogeochemistry. Atmos.
855   Chem. Phys. 10, 10875-10893.

Martin, J.H., 1990. Glacial-interglacial CO2 change: The iron hypothesis. Paleoceanography 5, 1-13.

McConnell, J.R., Aristarain, A.J., Banta, J.R., Edwards, P.R., Simoes, J.C., 2007. 20th-Century doubling in dust archived in an Antarctic Peninsula ice core parallels climate change and desertification in South America. Proc. Natl. Acad. Sci. U. S. A. 104, 5743-5748.

860   Menut, L., Perez, C., Haustein, K., Bessagnet, B., Prigent, C., Alfaro, S., 2013. Impact of surface roughness and soil texture on mineral dust emission fluxes modeling. Journal of Geophysical Research-Atmospheres 118, 6505-6520.

Miller, R.L., et al., 2006. Mineral dust aerosols in the NASA goddard institute for Space Sciences ModelE atmospheric general circulation model. J. Geophys. Res.-Atmos. 111, D06208.

Miller, R.L., Knippertz, P., Pérez García-Pando, C., Perlwitz, J.P., Tegen, I., 2014. Impact of Dust Radiative Forcing upon
865   Climate, in: Knippertz, P., Stuut, J.-B.W. (Eds.), Mineral Dust: A Key Player in the Earth System. Springer Netherlands, Dordrecht, pp. 327-357.

Mosley-Thompson, E., Thompson, L.G., Grootes, P., Gundestrup, N., 1990. Little ice age (neoglacial) paleoenvironmental conditions at siple station, Antarctica. J. Glaciol. 14, 199-204.

Myriokefalitakis, S., et al., 2018. Reviews and syntheses: the GESAMP atmospheric iron deposition model intercomparison
870   study. Biogeosciences 15, 6659-6684.

O'Sullivan, D., et al., 2020. Models transport Saharan dust too low in the atmosphere: a comparison of the MetUM and CAMS forecasts with observations. Atmos. Chem. Phys. 20, 12955-12982.

Okin, G.S., 2008. A new model of wind erosion in the presence of vegetation. Journal of Geophysical Research-Earth Surface 113, F02s10.

875   Okin, G.S., Mahowald, N., Chadwick, O.A., Artaxo, P., 2004. Impact of desert dust on the biogeochemistry of phosphorus in terrestrial ecosystems. Global Biogeochemical Cycles 18, Gb2005.

Omar, A., et al., 2010. Extinction-to-backscatter ratios of Saharan dust layers derived from in situ measurements and CALIPSO overflights during NAMMA. Journal of Geophysical Research-Atmospheres 115.

Painter, T.H., Deems, J.S., Belnap, J., Hamlet, A.F., Landry, C.C., Udall, B., 2010. Response of Colorado River runoff to
880   dust radiative forcing in snow. Proc. Natl. Acad. Sci. U. S. A. 107, 17125-17130.

Pantillon, F., Knippertz, P., Marsham, J.H., Birch, C.E., 2015. A Parameterization of Convective Dust Storms for Models with Mass-Flux Convection Schemes. J. Atmos. Sci. 72, 2545-2561.

Pérez Garcia-Pando, C., Miller, R.L., Perlwitz, J.P., Rodriguez, S., Prospero, J.M., 2016. Predicting the mineral composition of dust aerosols: Insights from elemental composition measured at the Izana Observatory. Geophysical Research Letters
885   43, 10520-10529.

Perlwitz, J.P., Perez Garcia-Pando, C., Miller, R.L., 2015a. Predicting the mineral composition of dust aerosols - Part 1: Representing key processes. Atmos. Chem. Phys. 15, 11593-11627.

Perlwitz, J.P., Perez Garcia-Pando, C., Miller, R.L., 2015b. Predicting the mineral composition of dust aerosols - Part 2: Model evaluation and identification of key processes with observations. Atmospheric Chemistry and Physics 15, 11629-11652.

Petit, J.R., et al., 1999. Climate and atmospheric history of the past 420,000 years from the Vostok ice core, Antarctica. Nature 399, 429-436.

Prospero, J.M., Barkley, A.E., Gaston, C.J., Gatineau, A., Sansano, A.C.Y., Panechou, K., 2020. Characterizing and Quantifying African Dust Transport and Deposition to South America: Implications for the Phosphorus Budget in the Amazon Basin. Global Biogeochemical Cycles 34.

Prospero, J.M., Ginoux, P., Torres, O., Nicholson, S.E., Gill, T.E., 2002. Environmental characterization of global sources of atmospheric soil dust identified with the Nimbus 7 Total Ozone Mapping Spectrometer (TOMS) absorbing aerosol product. Reviews of Geophysics 40, 1002.

Randles, C.A., et al., 2017. The MERRA-2 Aerosol Reanalysis, 1980 Onward. Part I: System Description and Data Assimilation Evaluation. Journal of Climate 30, 6823-6850.

Ridgwell, A.J., Watson, A.J., 2002. Feedback between aeolian dust, climate, and atmospheric CO2 in glacial time. Paleoceanography 17.

Ridley, D.A., Heald, C.L., Kok, J.F., Zhao, C., 2016. An observationally-constrained estimate of global dust aerosol optical depth. Atmos. Chem. Phys. 16, 15097-15117.

Ridley, D.A., Heald, C.L., Pierce, J.R., Evans, M.J., 2013. Toward resolution-independent dust emissions in global models: Impacts on the seasonal and spatial distribution of dust. Geophysical Research Letters 40, 2873-2877.

Rind, D., et al., 2020. GISS Model E2.2: A Climate Model Optimized for the Middle Atmosphere-Model Structure, Climatology, Variability, and Climate Sensitivity. Journal of Geophysical Research-Atmospheres 125.

Ryder, C.L., Highwood, E.J., Walser, A., Seibert, P., Philipp, A., Weinzierl, B., 2019. Coarse and giant particles are ubiquitous in Saharan dust export regions and are radiatively significant over the Sahara. Atmospheric Chemistry and Physics 19, 15353-15376.

Sarangi, C., Qian, Y., Rittger, K., Leung, L.R., Chand, D., Bormann, K.J., Painter, T.H., 2020. Dust dominates high-altitude snow darkening and melt over high-mountain Asia. Nature Climate Change 10, 1045-+.

Scanza, R., et al., 2015. Modeling dust as component minerals in the Community Atmosphere Model: development of framework and impact on radiative forcing. Atmos. Chem. Phys. 15, 537-561.

Schepanski, K., Tegen, I., Todd, M.C., Heinold, B., Bonisch, G., Laurent, B., Macke, A., 2009. Meteorological processes forcing Saharan dust emission inferred from MSG-SEVIRI observations of subdaily dust source activation and numerical models. Journal of Geophysical Research-Atmospheres 114.

Schroth, A.W., Crusius, J., Sholkovitz, E.R., Bostick, B.C., 2009. Iron solubility driven by speciation in dust sources to the ocean. Nature Geoscience 2, 337-340.

Seinfeld, J.H., et al., 2004. ACE-ASIA - Regional climatic and atmospheric chemical effects of Asian dust and pollution. Bull. Am. Meteorol. Soc. 85, 367-380.

Shao, Y., 2001. A model for mineral dust emission. Journal of Geophysical Research-Atmospheres 106, 20239-20254.

Shao, Y.P., 2008. Physics and Modelling of Wind Erosion, 2nd ed. Springer, Heidelberg.

Shao, Y.P., et al., 2011. Dust cycle: An emerging core theme in Earth system science. Aeolian Research 2, 181-204.

Sharma, D., Miller, R.L., 2017. Revisiting the observed correlation between weekly averaged Indian monsoon precipitation and Arabian Sea aerosol optical depth. Geophysical Research Letters 44, 10006-10016.

Shi, Y., Liu, X.H., 2019. Dust Radiative Effects on Climate by Glaciating Mixed-Phase Clouds. Geophysical Research Letters 46, 6128-6137.

Shindell, D.T., et al., 2013. Radiative forcing in the ACCMIP historical and future climate simulations. Atmospheric Chemistry and Physics 13, 2939-2974.

Skiles, S.M., Flanner, M., Cook, J.M., Dumont, M., Painter, T.H., 2018. Radiative forcing by light-absorbing particles in snow. Nature Climate Change 8, 965-+.

Souney, J.M., et al., 2002. A 700-year record of atmospheric circulation developed from the Law Dome ice core, East Antarctica. Journal of Geophysical Research-Atmospheres 107.

Stanelle, T., Bey, I., Raddatz, T., Reick, C., Tegen, I., 2014. Anthropogenically induced changes in twentieth century mineral dust burden and the associated impact on radiative forcing. Journal of Geophysical Research-Atmospheres 119, 13526-13546.

Storelvmo, T., 2017. Aerosol Effects on Climate via Mixed-Phase and Ice Clouds. Annual Review of Earth and Planetary Sciences, Vol 45 45, 199-222.

Swap, R., Garstang, M., Greco, S., Talbot, R., Kallberg, P., 1992. Saharan dust in the amazon basin. Tellus Ser. B-Chem. Phys. Meteorol. 44, 133-149.

Tanaka, T.Y., Chiba, M., 2006. A numerical study of the contributions of dust source regions to the global dust budget. Glob. Planet. Change 52, 88-104.

Tegen, I., Werner, M., Harrison, S.P., Kohfeld, K.E., 2004. Relative importance of climate and land use in determining present and future global soil dust emission. Geophysical Research Letters 31.

van der Does, M., et al., 2020. Tropical Rains Controlling Deposition of Saharan Dust Across the North Atlantic Ocean. Geophysical Research Letters 47.

Vergara-Temprado, J., et al., 2018. Strong control of Southern Ocean cloud reflectivity by ice-nucleating particles. Proc. Natl. Acad. Sci. U. S. A. 115, 2687-2692.

Vinoj, V., Rasch, P.J., Wang, H.L., Yoon, J.H., Ma, P.L., Landu, K., Singh, B., 2014. Short-term modulation of Indian summer monsoon rainfall by West Asian dust. Nature Geoscience 7, 308-313.

Warren, A., et al., 2007. Dust-raising in the dustiest place on earth. Geomorphology 92, 25-37.

Washington, R., et al., 2009. Dust as a tipping element: The Bodele Depression, Chad. Proc. Natl. Acad. Sci. U. S. A. 106, 20564-20571.

Weinzierl, B., et al., 2017. The Saharan Aerosol Long-range Transport and Aerosol-Cloud Interaction Experiment (SALTRACE): overview and selected highlights. Bull. Am. Meteorol. Soc. 98, 1427-1451.

Wong, L.T., Chow, W.K., 2001. Solar radiation model. Applied Energy 69, 191-224.

Wu, C.C., Lin, Z., Liu, X., 2020. The global dust cycle and uncertainty in CMIP5 (Coupled Model Intercomparison Project phase 5) models. Atmospheric Chemistry and Physics 20, 10401-10425.

Xu, H., Zheng, F.J., Zhang, W.H., 2016. Variability in Dust Observed over China Using A-Train CALIOP Instrument. Adv. Meteorol., 11.

Yorks, J.E., et al., 2014. The Airborne Cloud-Aerosol Transport System: Overview and Description of the Instrument and Retrieval Algorithms. Journal of Atmospheric and Oceanic Technology 31, 2482-2497.

Yu, H.B., Chin, M., Winker, D.M., Omar, A.H., Liu, Z.Y., Kittaka, C., Diehl, T., 2010. Global view of aerosol vertical distributions from CALIPSO lidar measurements and GOCART simulations: Regional and seasonal variations. Journal of Geophysical Research-Atmospheres 115.

Yu, H.B., et al., 2015. The fertilizing role of African dust in the Amazon rainforest: A first multiyear assessment based on data from Cloud-Aerosol Lidar and Infrared Pathfinder Satellite Observations. Geophysical Research Letters 42, 1984-1991.

Yu, H.B., et al., 2019. Estimates of African Dust Deposition Along the Trans-Atlantic Transit Using the Decadelong Record of Aerosol Measurements from CALIOP, MODIS, MISR, and IASI. Journal of Geophysical Research-Atmospheres 124, 7975-7996.

Yu, Y., et al., 2020. Disproving the Bodele Depression as the Primary Source of Dust Fertilizing the Amazon Rainforest. Geophysical Research Letters 47.

Zhang, Y., et al., 2015. Modeling the global emission, transport and deposition of trace elements associated with mineral dust. Biogeosciences 12, 5771-5792.